SANDIA REPORT

SAND2005-3000
Unlimited Release
Printed May 2005

Progress Report for the ASCI AD Resistance Weld Process Modeling Project AD2003-15

W. S. Winters
Engineering Mechanics Modeling & Simulation Department 8774

A. A. Brown, D. J. Bammann and J. W. Foulk III
Science Based Material Modeling Department 08763

A. R. Ortega
W80 System Design Qualification Department 08242

Prepared by
Sandia National Laboratories
Albuquerque, New Mexico 87185 and Livermore, California 94550

Sandia is a multiprogram laboratory operated by Sandia Corporation,
a Lockheed Martin Company, for the United States Department of Energy's
National Nuclear Security Administration under Contract DE-AC04-94-AL85000.

Sandia National Laboratories

Issued by Sandia National Laboratories, operated for the United States Department of Energy by Sandia Corporation.

Available to DOE and DOE contractors from
U.S. Department of Energy
Office of Scientific and Technical Information
P.O. Box 62
Oak Ridge, TN 37831

Telephone:	(865) 576-8401
Facsimile:	(865) 576-5728
E-Mail:	reports@adonis.osti.gov
Online ordering:	http://www.doe.gov/bridge

Available to the public from
U.S. Department of Commerce
National Technical Information Service
5285 Port Royal Rd
Springfield, VA 22161

Telephone:	(800) 553-6847
Facsimile:	(703) 605-6900
E-Mail:	orders@ntis.fedworld.gov
Online order:	http://www.ntis.gov/help/ordermethods.asp?loc=7-4-0#online

SAND2005-3000
Unlimited Release
Printed May 2005

Progress Report for the ASCI AD Resistance Weld Process Modeling Project AD2003-15

W. S. Winters
Engineering Mechanics Modeling & Simulation Department 8774

A. A. Brown, D. J. Bammann and J. W. Foulk III
Science Based Material Modeling Department 08763

A. R. Ortega
W80 System Design Qualification Department 08242

Sandia National Laboratories
Livermore, California 94551-0969

Abstract

This report documents activities related to the ASCI AD Resistance Weld Process Modeling Project AD2003-15. Activities up to and including FY2004 are discussed. This was the third year for this multi year project, the objective of which is to position the SIERRA computational tools for the solution of resistance welding problems. The process of interest is a three-way coupled problem involving current flow, temperature buildup and large plastic deformation. The DSW application is the reclamation stem weld used in the manufacture of high pressure gas bottles. This is the first year the CALAGIO suite of codes (eCALORE, CALORE, and ADAGIO) was used to successfully solve a three-way coupled problem in SIERRA. This report discusses the application of CALAGIO to the tapered bar acceptance problem and a similar but independent tapered bar simulation of a companion C6 experiment. New additions to the EMMI constitutive model and issues related to CALAGIO performance are also discussed.

Acknowledgements

The authors would like to acknowledge the support of the Sierra code development team including Steve Bova, 09141, Jason Hales, 09142, John Mitchell, 02614, Nathan Crane, 09142, and Kendall Pierson, 09142. The authors would also like to acknowledge the contributions of our C6 experimental team, Jerry Knorovsky, 1833 and Bonnie Antoun, 8754. Finally, the authors would like to thank our DSW customer, Steve Robinson, 08243 for his insight into the resistance welding process and his interest in developing a comprehensive model.

Contents

List of Figures

List of Tables

This page intentionally left blank

1 Introduction

The purpose of this report is to document activities related to the Resistance Weld Process Modeling ASCI AD Project AD2003-15. The body of this report will discuss work performed in FY2004. Work prior to FY2004 is discussed in Appendix A.

This project is a modeling effort designed to stimulate code enhancements that will position SIERRA for the analysis of resistance welding problems important to Sandia. The project represents the focal point of collaboration between the DSW customer, the SIERRA programming team, analysts, and C6 experimental activities. This is the third year of the multi-year Resistance Welding ASCI AD project.

1.1 Motivation and Background

Resistance welding is used in the final steps of the complicated and expensive GTS reservoir manufacturing process. Post-weld cracking has been observed in reservoirs following exposure to high-pressure tritium. Cracking has been traced to material degradation due to long term exposure to tritium, in conjunction with high residual stresses. Since cracks have the potential of growing through a reservoir wall and releasing tritium, we must better understand the stress state imparted to the material in the region of these solid-state (weld) bonds. This project augments experimental efforts to characterize bond properties by extending our predictive capabilities and enabling optimization of bond properties. Post-weld cracking in tritium reservoirs is a potential Price Anderson Amendment Act (PAAA) issue. Sandia's PAAA office has determined that we, as a laboratory, are in compliance as long as we are working to understand and mitigate the problem. The Resistance Weld Process Modeling AD Project is a significant part of the GTS weld characterization, and thus a critical element in our maintaining compliance with PAAA.

This project seeks to develop resistance weld modeling tools that predict resistance heating, transient temperature distribution, material deformation, microstructural state, weld quality and residual stress in welded parts. Data from the literature and C6 resistance welding and material characterization tests will aid in tool development and ultimately provide the means of assessing both qualitative and quantitative predictive capability. These analysis tools will be applied to the GTS stem attachment weld, a DSW process of interest. A coupled electrical-thermal-mechanical SIERRA predictive capability for resistance welding is currently under development using CALAGIO (eCALORE, CALORE, and ADAGIO).

An important FY04 deliverable for this AD project was the CALAGIO solution of the tapered bar Acceptance Problem. This was the first SIERRA-based solution of a fully coupled electrical-thermal-mechanical problem of significant size that includes large plastic deformation and thermal softening. A new code feature, a mixed SD3DH8 element with thermal strain capability, was also tested in FY04. The SD3DH8 element is a higher order element and should enable more accurate models to be developed with fewer elements. In addition, two steps were completed toward our ultimate objective of simulating the solid-state bonding process by switching from sliding to tied contact based on the constitutive model. First, an enhanced version of the Evolving Microstructure Material Model for Inelasticity

(EMMI), formally referred to as the BCJ Model [1], was implemented and has the capability to model the processes of recrystallization and grain growth. Second, a regression test was added that will be used to test the upcoming ADAGIO feature to transition from sliding to tied contact. The solid-state bond model, together with the CALAGIO coupled electrical-thermal-mechanical code, form the basis for SIERRA modeling of the resistance welding process.

Sandia's need to develop a resistance weld modeling capability has resulted in the addition of a number of new features in SIERRA. Table 1 lists new features required to model resistance welding and their status with regard to implementation. This project leverages heavily against the Inertia Welding ASCI AD Project. Thus many of the features listed in Table 1 are relevant to both projects.

Table 1 New CALAGIO Features Required for Resistance Weld Modeling

Feature	Status
Partial coupling of CALORE & ADAGIO (Temperature increases in CALORE, impact ADAGIO material properties)	Completed
Full coupling of CALORE & ADAGIO (Heat of plastic work computed by ADAGIO becomes a heat source for CALORE)	Completed this year
ADAGIO slide-to-tied capability	Incomplete
Implementation of the solid state bond model including recrystallization and grain growth	Completed this year
Implementation of contact electrical resistance	Incomplete
Implementation of generalized friction model for contact surfaces	Incomplete
Implementation of remesh-remap-restart for the CALAGIO suite (may be needed for large strains near contact surfaces)	Need uncertain
Implementation of special elements for large strain near contact surfaces)	Need uncertain

1.2 Our Approach to Model Development

Sandia's resistance weld modeling capability is centered on the SIERRA code CALAGIO. CALAGIO is a driver that links ADAGIO, a quasistatic mechanics code and CALORE, a fully transient heat conduction code. When solving resistance welding problems, CALAGIO also drives a special version of CALORE called eCALORE to solve the electrical problem. During a resistance weld simulation, CALAGIO computes a converged solution for the mechanical, thermal and electrical problem at each time step. All solutions are performed on

an updated mesh that continues to change with time. The assumption is made that the thermal and electrical energy entering or leaving any element as a result of mesh movement over a time step is negligible. The component of thermal or electrical energy transport due to mesh movement is commonly referred to as convection. Hence CALAGIO neglects convection but fully accounts for thermal and electrical transport due to heat conduction and Ohm's law.

Resistance welding is a true tightly coupled thermal-electrical-mechanical problem. During a resistance weld, a voltage potential is placed across the two parts to be welded causing heat buildup in the area of highest electrical resistance, *i.e.*, the bond interface. Typically a load is also applied pressing the parts together at the bond interface. As resistive heating adjacent to the bond interface increases, the temperature rises, and the parts undergo thermal softening and large deformation. The increased temperatures causes recrystallization and grain growth across the bond interface leading to a solid state bond. In resistance welding neither part reaches a molten state.

In addition to accounting for coupled thermal-electrical-mechanical behavior in the welded components, an effective resistance weld modeling capability must treat electrical resistance and friction at the weld interface. The DSW problem of interest is the reclamation stem weld problem shown schematically in Figure 1. Resistance welding is used to weld the gas bottle fill stem into the gas bottle. During the weld an electrical potential is placed across the gas bottle and stem and an axial load is applied to the stem as it slides into place. Friction and electrical resistance at the sliding interface will affect local deformation and resistive heating in the weld zone.

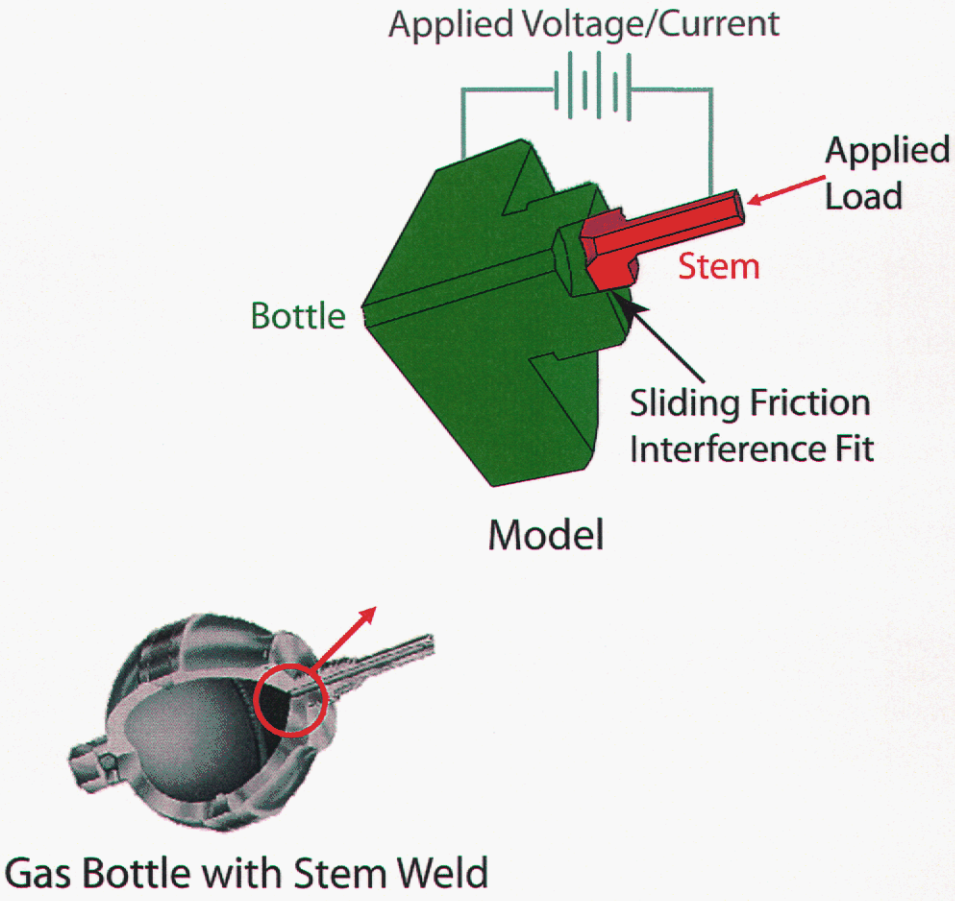

Figure 1 The reclamation stem weld

Our approach to developing a resistance weld modeling capability, allows us to add the complexities of interface electrical resistance and friction in stages. In order to accomplish this, we will simulate the two problems depicted in Figure 2a. Our computed results will be compared to companion C6 experiments and data from the literature. Each problem in Figure 2 makes use of an axisymmetric tapered bar geometry. In each case an electrical potential is placed across the ends of the tapered bar and an axial load is applied. Heat will build up at the narrowest part of the tapered bar causing thermal softening and large localized deformations. The tapered bar problem shown in the upper part of the figure is a thermal-electrical-mechanical problem with no weld interface. In the current project there are two forms of the tapered bar problem each with slightly different geometries and boundary conditions. The first of these is referred to here and in other project documentation as the "acceptance problem." Geometry and boundary conditions for the acceptance problem are based on an experiment conducted by Eggert and Dawson [2]. The second tapered bar simulation is based on a C6 experiment conducted in support of this project.

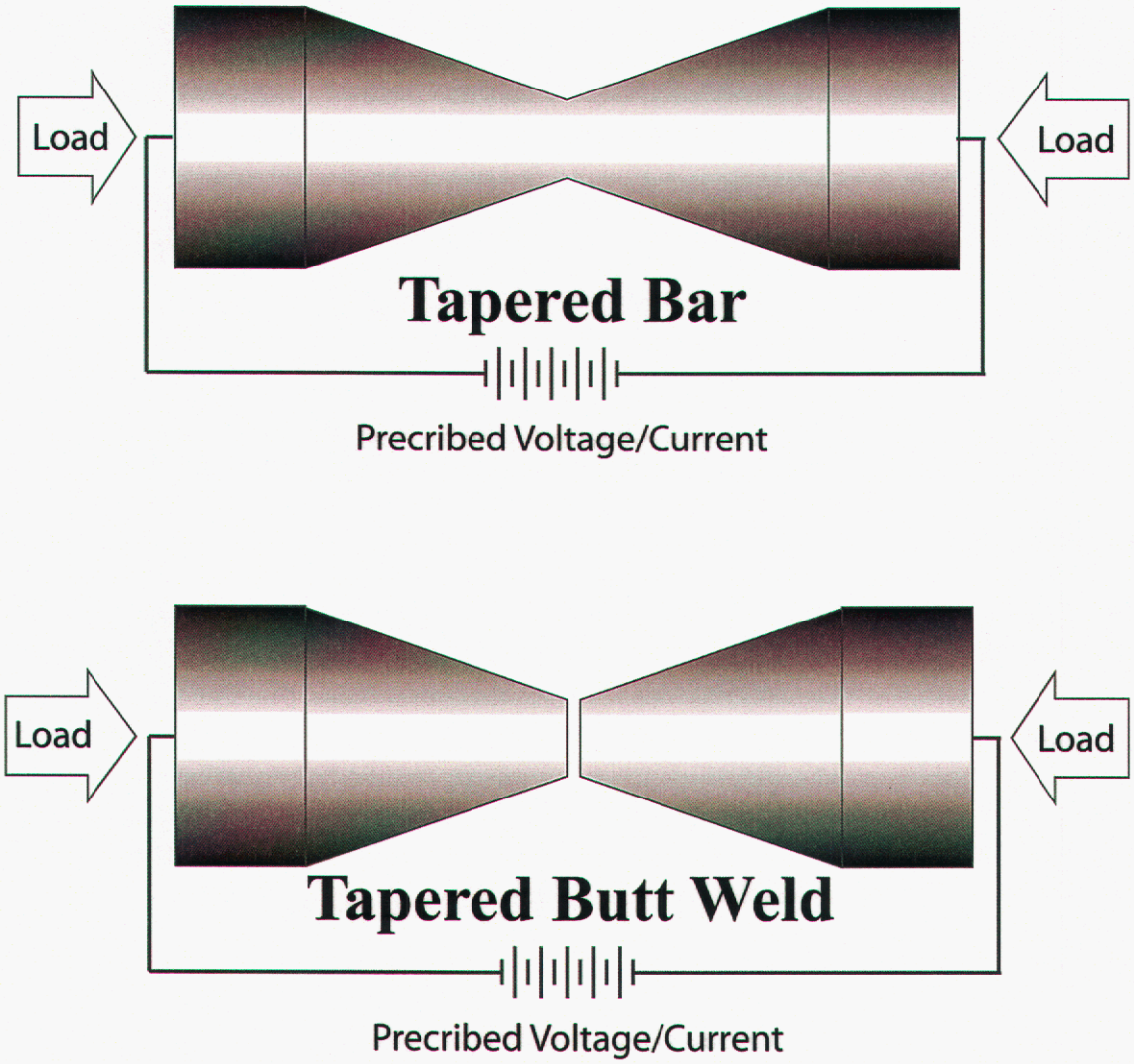

Figure 2 Tapered bar simulations

In the tapered butt weld problem shown in the lower part of the Figure 2, a weld interface is introduced but because of the axisymmetric nature of the problem, it is only necessary to consider the added complexity of interface electrical resistance since no sliding friction will be present during the weld. In addition to addressing interface electrical resistance, the tapered butt weld will also make use of the solid state bond model.

Once we have demonstrated a capability to model the tapered bar and tapered butt weld problems, we will be in a position to address the DSW problem of interest, the reclamation weld. The only new modeling complexity in the DSW problem will be interface friction.

1.3 Points of Contact

As mentioned previously, this project represents the focal point of collaboration between the DSW customer, the SIERRA programming team, analysts, and C6 experimental activities. Our DSW customer is Steve Robinson, 08243. The ASCI AD project team consists of Bill Winters, 08752 and Arthur Brown, 08763. The SIERRA programming team for FY04 included Steve Bova, 09141, Jason Hales, 09142, John Mitchell, 02614, Nathan Crane, 09142, and Kendall Pierson, 09142. Our project receives experiment support from Jerry Knorovsky, 01833 and Bonnie Antoun, 08754 who are funded under C6.

1.4 Schedule and Tasks

Figure 3 depicts task scheduling for the Resistance Weld Process Modeling ASCI AD Project in Gantt Chart form. Scheduling of originally planned tasks are shown as black bars. In some cases completion of these tasks was extended during the course of the year. These extensions are shown as white bars. Completed tasks are shown with the letter "C." Task dependencies are indicated with vertical arrows. For example, Task 5 (Obtain a mesh independent solution of the acceptance problem) could not be completed until Task 2 (First solution of the acceptance problem on a coarse grid) is complete.

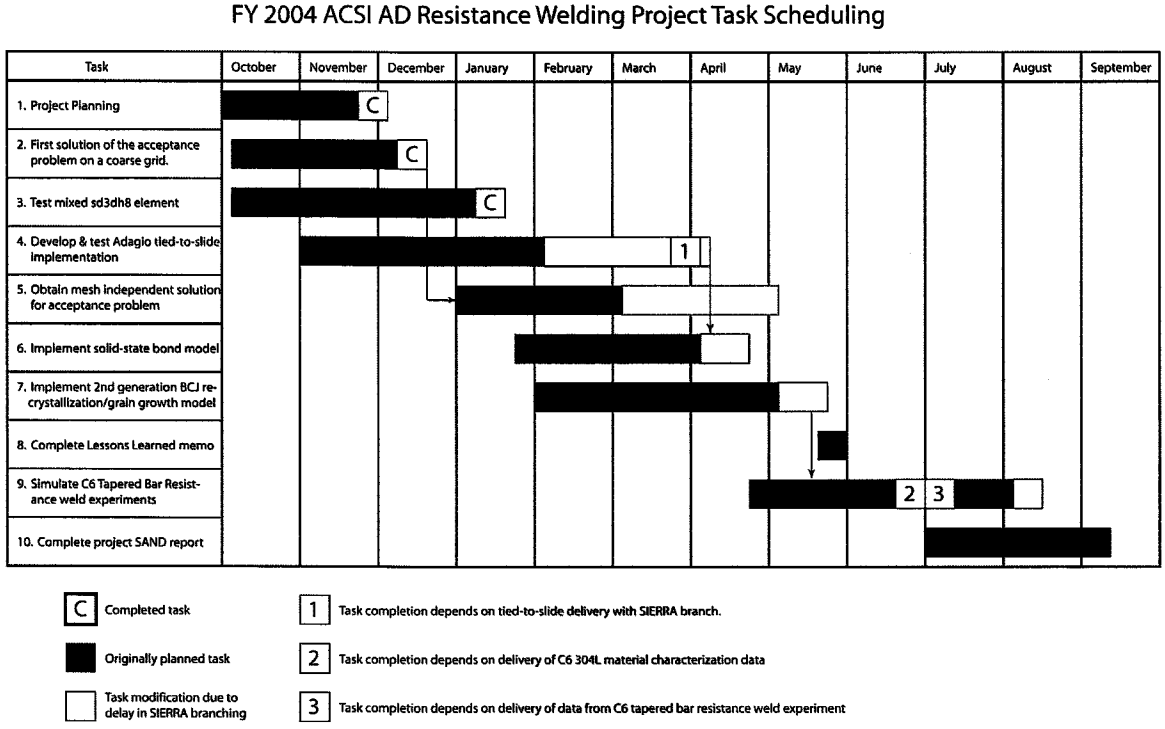

Figure 3 Resistance weld modeling Gantt chart for FY2004

Task completion delays were caused by "unplanned" activities related to the implementation of the SIERRA framework. In the first and second quarters of FY04, unforeseen problems and delays in refactoring were the principle contributors to schedule modification. During refactoring, SIERRA programmer priorities were shifted to framework issues and away from the addition of new code features. Refactoring delays impacted tasks 4-7 and to a lesser extent, task 9.

Two tasks remained uncompleted in FY2004, tasks 4 and 9. Task 4 was delayed due to the SIERRA refactoring as well as personnel changes in the Adagio development team. Even so, a regression test has been created to test the capability once it has been implemented (see Section 4). In Task 9, a simulation of the C6 tapered bar experiment was to be compared to data. Completion of this task was delayed into FY2005 because of convergence issues with CALORE/eCALORE and problems in obtaining accurate C6 data.

1.5 Report Overview

Section 2 of this report describes the solution of the acceptance problem. Convergence issues related to CALAGIO are also discussed. In Section 3 studies conducted with the new SD3DH8 element are documented. Activities related to improving the EMMI model for resistance welding applications are discussed in Section 4. Section 5 describes the Sandia tapered bar problem and presents some preliminary results. Concluding remarks are given in Section 6.

This page intentionally left blank

2 Solution of the Acceptance Problem

This section documents our efforts to solve the tapered bar "acceptance problem." The acceptance problem is a tapered bar simulation so named because it demonstrates the capability to solve three-way coupled (thermal-electrical-mechanical) problems in the SIERRA framework.

2.1 Description of the Acceptance Problem

The acceptance problem is modeled after a set of tapered bar experiments conducted by Eggert and Dawson [2-4]. They applied a prescribed axial load and voltage potential across the ends of a tapered bar and measured the resulting upset (relative axial displacement of bar ends) and temperature distribution as a function of time. The final deformed shape of the tapered bar was also measured. Their data has been available as an aid in validating models for three-way coupled simulations since the mid 1980's. At Sandia, Ortega *et. al.* [5, 6] have utilized this data to evaluate the three-way modeling capability using the codes TORO (electrical), COYOTE (thermal) and JAS (structural). Their work is documented in Appendix A. The present work represents the first use of this data to evaluate the CALAGIO suite (CALORE, eCALORE and ADAGIO) in SIERRA.

The dimensions of the Eggert-Dawson tapered bar sample are shown in Figure 4. The 304 stainless steel specimen is approximately 42 mm long and tapers to a diameter of 5 mm at its center. The diameter of the straight sections is approximately 13 mm. The 5 mm "waist" ensures that the resistance heating will be localized near the center of the tapered bar.

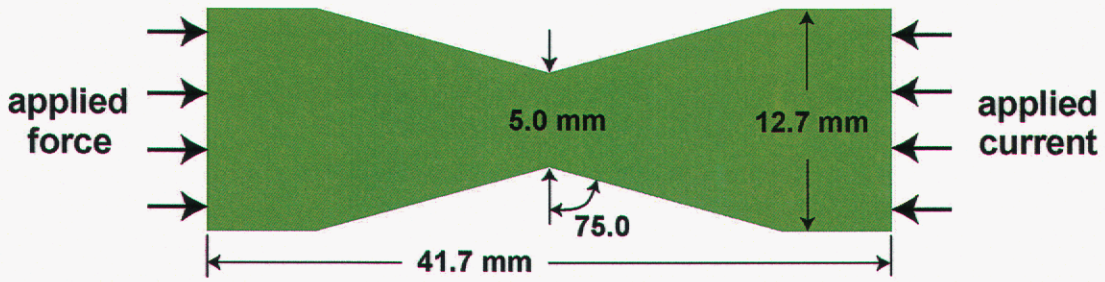

Figure 4 The tapered bar specimen for the acceptance problem

Figure 5 shows the time dependent current and axial load applied to the ends of the tapered bar. These represent the boundary conditions for the three-way coupled problem. A large array of automotive car batteries were used as the electrical source and the current was carefully measured as a function of time. Eggert and Dawson's computed voltage drop across the straight sections of the tapered bar compared favorably to independently measured values thus adding credibility to their measured electrical boundary condition (see, *e.g.* [2]).

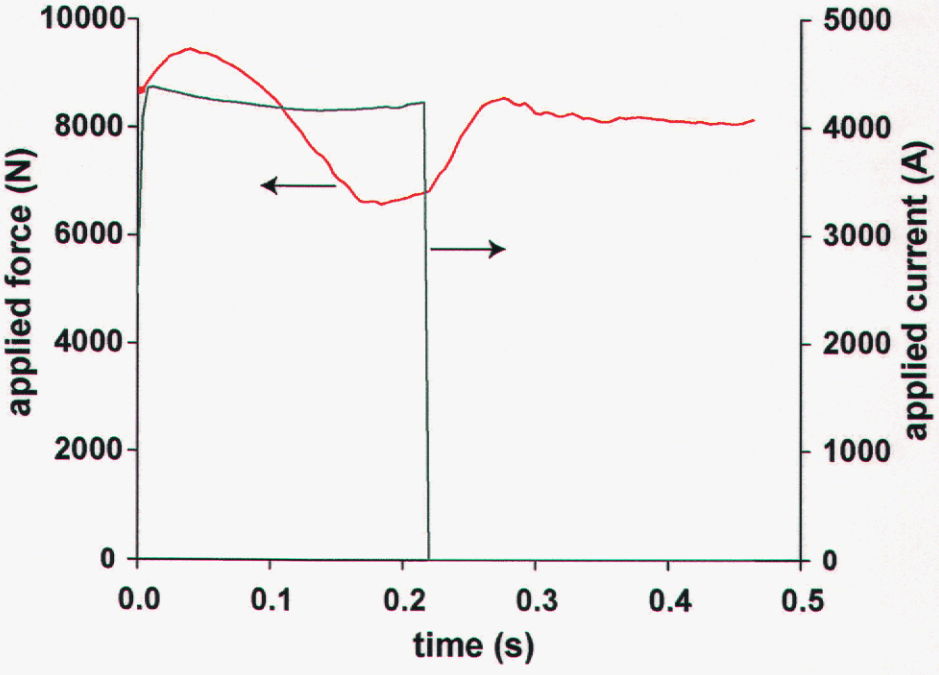

Figure 5 Electrical and mechanical boundary conditions for the acceptance problem

2.2 Results

Several tapered bar meshes were prepared for simulation using CALAGIO. Statistics regarding these meshes are summarized in Table 2. Also shown in the table are processor partitioning and resulting run times on the Sandia Shasta Institutional Cluster. The coarse mesh for the acceptance problem is shown in Figure 6. This mesh, like all meshes for our axisymmetric tapered bar simulations, makes use of symmetry boundary conditions to reduce the number of grids. The axisymmetric nature of the problem is discussed in greater detail in Section 5.

Table 2 Meshing Details for the Acceptance Problem

mesh	elements	nodes	processors	walltime (hr)	total CPU time (hr)
very coarse	1304	1703	4	0.3	1.1
coarse	9461	10995	8	1.6	12.5
medium	28426	31599	8	6.0	48.1
fine	233640	246408	32	28.9	924.8
very fine	1076290	1111632	72	96.0	6910.8

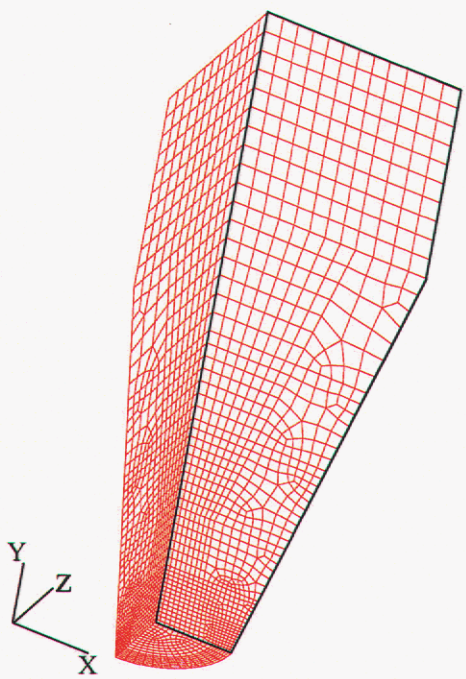

Figure 6 Coarse mesh for the acceptance problem

The final deformed mesh for a simulation of the medium grid acceptance problem is shown in Figure 7. Large deformations are evident near the center of the tapered bar. These deformations are caused by the localized resistive heating which results in thermal softening of the material. Under the presence of the axial load, large deformations occur resulting in the "bulge" of material at the center.

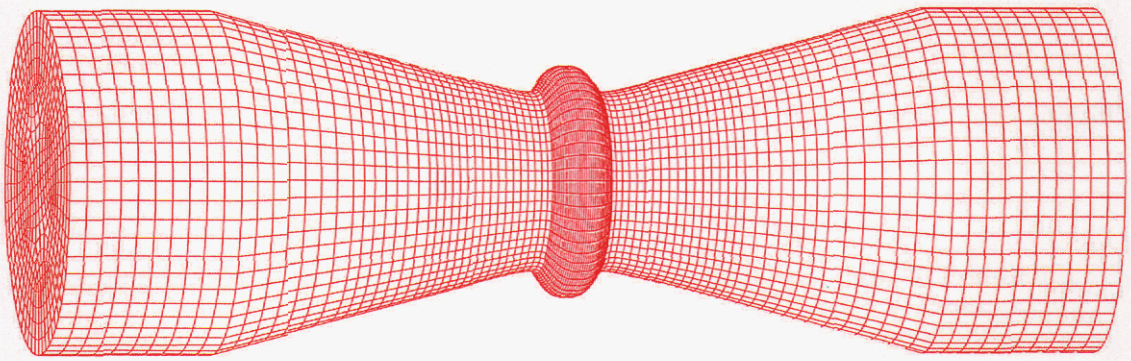

Figure 7 Deformed mesh for the acceptance problem

Figure 8 shows how the Eggert-Dawson measurements compares to ADAGIO computed results with the very fine mesh. The upper figure shows measured and computed surface temperatures at thermocouple location T2. This location is near the waist of the sample. The center figure is a similar comparison for thermocouple location T4, slightly farther away from the waist. The lower figure shows measured and computed upset as a function of time. The upset is the reduction in axial length from the top surface to the waist.

Although the Resistance Weld Process Modeling Project is not a V&V project, we made an attempt to examine the influence of time step and mesh size on the computed solution of the acceptance problem. Figure 9 illustrates the influence of time step for the coarse mesh. The upper figure shows the computed upset as a function of time. The center figure shows the transient radial displacement of a surface node at the waist of the tapered bar. The lower figure shows the computed transient surface temperature at thermocouple location T1 (near the waste). The time steps used in this comparison are shown in the plots and range between .0025 and .00005 seconds. The results show that only negligible improvement in the mechanical part of the solution occurs for time steps less than .00025 seconds. The predicted surface temperature in the lower figure does not appear to improve significantly for time steps lower than .001 seconds.

Figure 10 illustrates the influence of mesh size on the convergence of the acceptance problem. Axial displacement and the surface temperature at thermocouple location T1 were compared for the five different meshes. The results show that as the mesh is refined, the solutions appear to be converging to a point where the results would be indifferent to further mesh refinement. Both the upset and the temperature appear almost identical for the fine and very fine meshes.

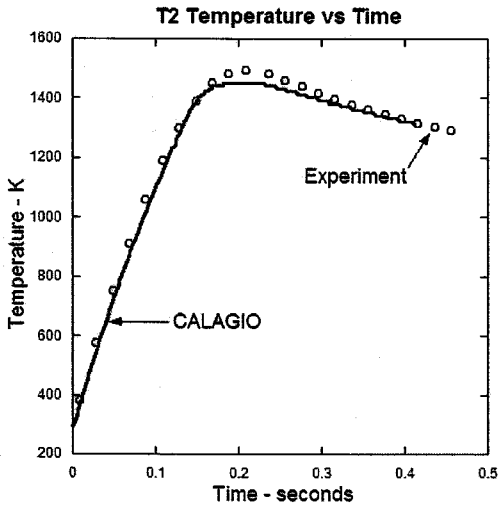

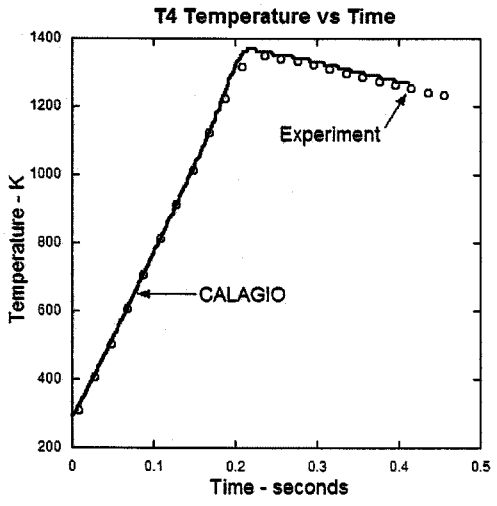

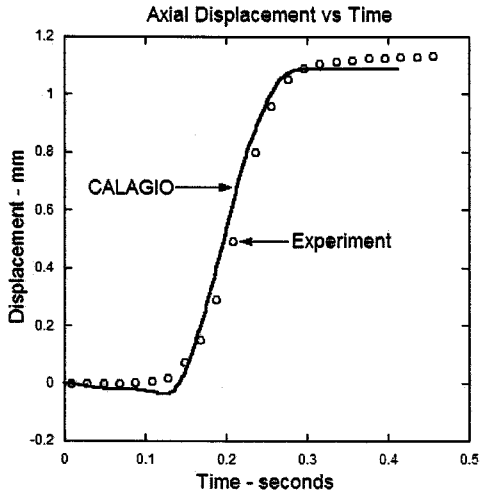

Figure 8 Measured and computed parameters for the acceptance problem

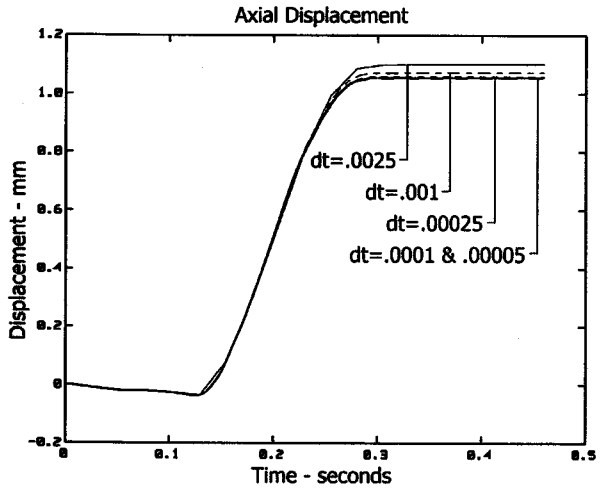

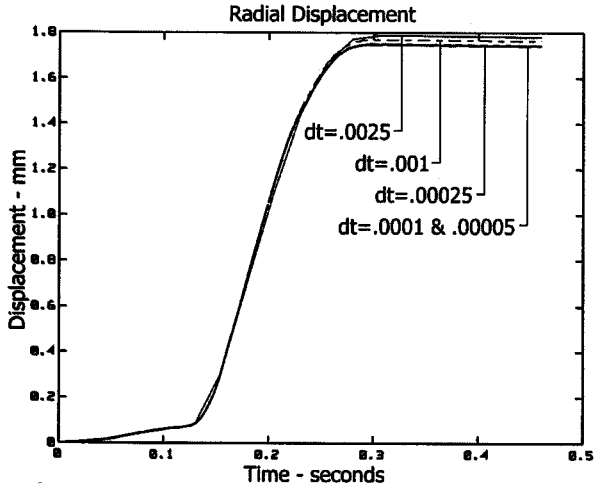

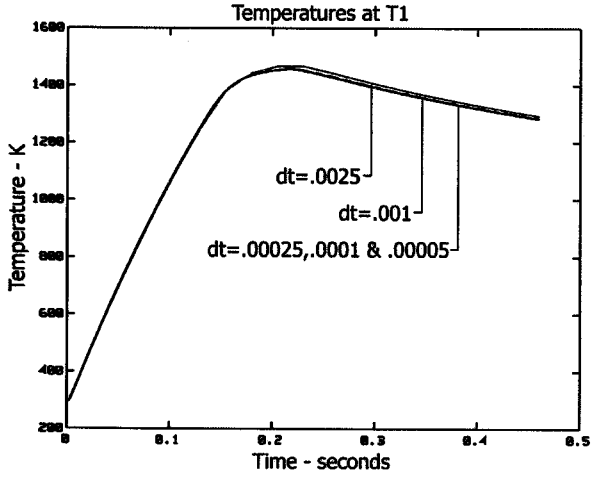

Figure 9 Influence of time step in simulating the acceptance problem

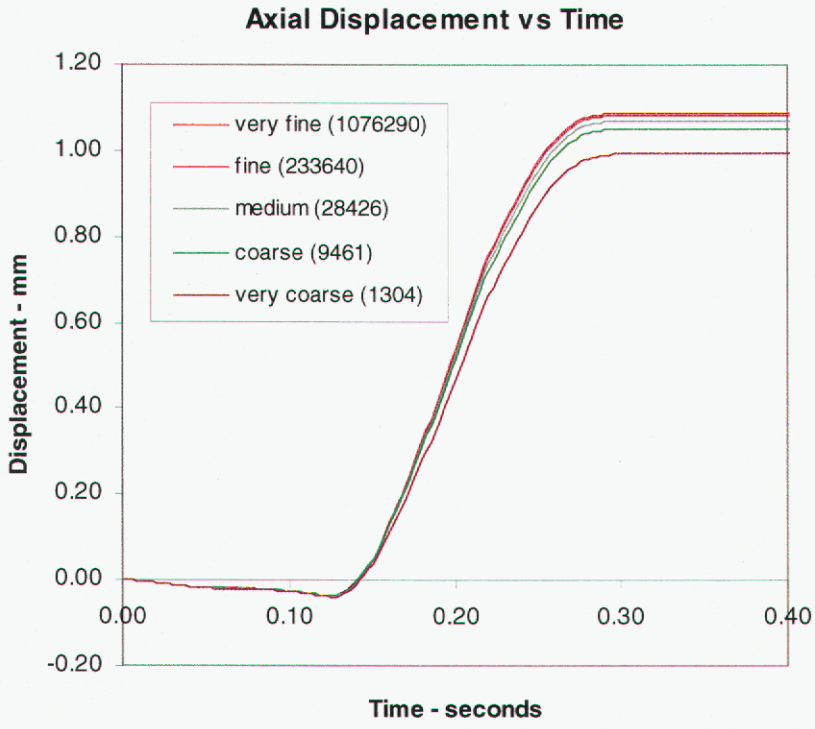

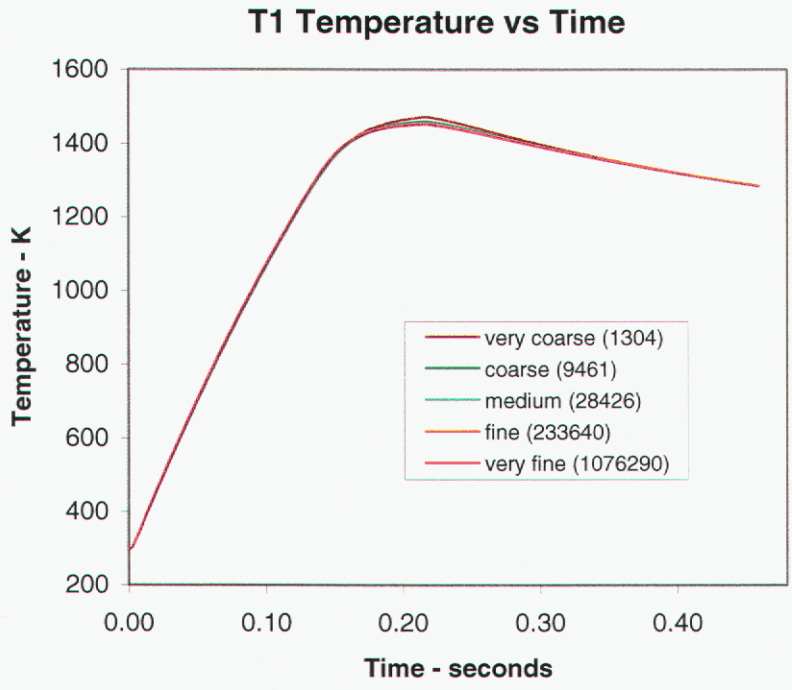

Figure 10 Influence of mesh size in simulating the acceptance problem

This page intentionally left blank

3 SD3DH8 Element Studies and Convergence Issues

Early in FY2004, we were having considerable difficulties getting the acceptance problem to run to completion. The simulations always failed due to either hourglassing or a lack of convergence. At first, we considered two possible solutions to these issues: 1) allow the elastic moduli used by the preconditioner in the Adagio conjugate gradient algorithm to depend on temperature; and 2) use of the selective deviatoric (SD3DH8) element. The former solution was postulated because the temperatures in the acceptance problem increase to near-melt, which dramatically reduces the values of the elastic moduli in the constitutive model. The necessary modifications to the preconditioner were made, but the hourglassing and lack of convergence continued to be an issue. We then turned to the selective deviatoric element.

The SD3DH8 is a higher order element, so it has the potential to reduce the number of elements required to achieve a sufficiently accurate solution. Another advantage is that, because it uses a combination of mean quadrature and a full integration, the selective deviatoric element can provide hourglass control without artificial hourglass parameters (see [7]). The bulk response is determined solely by mean quadrature, but a deviatoric parameter controls how much of the deviatoric response is taken from a uniform gradient integration and how much is taken from a full integration of the element. A value of 0.0 for the deviatoric parameter gives a pure uniform gradient response with no hourglass control. A value of 1.0 gives a fully-integrated deviatoric response. Any value between 0.0 and 1.0 can be used, but lower values are generally preferred.

We tried using the SD3DH8 element with the full range of values for the deviatoric parameter, but consistently observed hourglassing (see Figure 11). Although the ADAGIO developers (*e.g.* Jason Hales *et. al.*) were able to reduce the hourglassing seen with the SD3DH8 element by using a more uniform, refined mesh, we find that some hourglassing still occurs in regions of highest strain. It appears that the selective deviatoric element is extremely sensitive to the mesh quality and coarseness.

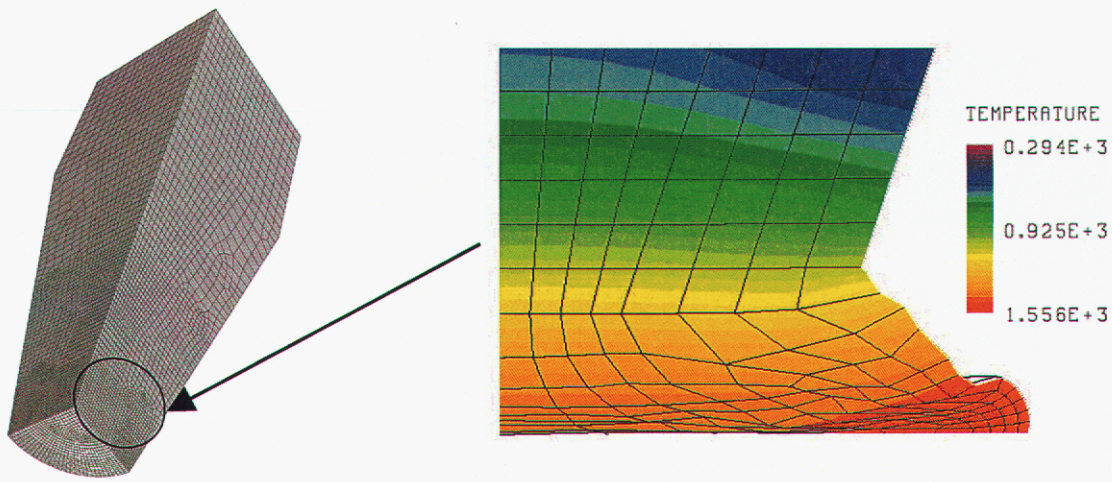

Figure 11 Hourglassing exhibited by the selective deviatoric element

In addition to studies using the SD3DH8 element, a matrix of problems was run using the under-integrated (UG3DH8) single point quadrature element with various values of parameters related to element strain formulation, preconditioner type, and hourglass control. We found that whenever the strongly objective strain formulation was used, either hourglassing or the lack of convergence errors occurred. When the midpoint-increment strain formulation was used, neither of these problems arose and stable solutions were achieved. This finding was reported to the SIERRA developers. As a result, an error was discovered in the calculation of effective moduli used in hourglass routines with the strongly objective strain formulation. The error has been fixed. As of now, the under-integrated element is satisfying our needs and is providing stable solutions free of hourglassing.

We will continue to work with the SIERRA developers to try to understand and improve the SD3DH8 element, but until the hourglassing issue is resolved, we will maintain our focus on the under-integrated element.

4 Constitutive Modeling

In the resistance welding process, current flow induces a temperature rise that leads to thermal softening, plastic deformation, recrystallization, and grain growth, and ultimately results in atomic bonding across the weld interface. Bond quality in resistance welds is assessed based on the bond length and the level of recrystallization and grain growth across the interface.

To model the solid-state bonding process (for example, in the tapered butt weld problem) we plan to transition from sliding to tied contact at the weld interface when the constitutive model determines that a critical amount of recrystallization has occurred. When the critical level is achieved in the interface elements, the corresponding nodes will be tied across the interface, effectively "welding" the surfaces together. To meet these needs, the EMMI constitutive model has been modified to track the evolution of recrystallization and grain growth. Although the acceptance problem simulations were all run using the classic BCJ model, the enhanced version described in this section will be required for the butt weld and reclamation stem weld simulations to be performed in FY05.

4.1 Necessary Model Modifications

The classic BCJ elasto-viscoplasticity theory is a thermodynamically consistent internal state variable model that includes a scalar isotropic hardening variable as well as a back stress tensor (see [1, 8]). The evolution equations for these two variables are motivated by dislocation mechanics, and account for dislocation generation as well as recovery mechanisms.

For the purposes of this project, the model has been enhanced to capture the effects of recrystallization and grain growth. Recrystallization occurs through a nucleation and growth process. During plastic deformation, geometrically necessary dislocations accumulate in subgrain boundaries. At high temperatures, it can be energetically favorable for subgrains with relatively low dislocation density to form recrystallization nuclei. These nuclei grow at the expense of neighboring regions, sweeping away the surrounding dislocation structure and hence resulting in a decrease in the yield strength. After a material is fully recrystallized, the grains continue to grow in an effort to minimize grain boundary energy. To model the recrystallization and grain growth processes, variables were added to the constitutive model to represent the volume fraction of recrystallized material and the average grain size.

In the modified version of the model, the rate of plastic deformation is given by

$$\boldsymbol{d}^p = \sqrt{\frac{3}{2}} f(\theta) \left(\sinh \left[\left\langle \frac{\sqrt{\frac{3}{2}} \|\boldsymbol{\xi}\|}{\left(\kappa + Y(\theta)(1 + \frac{c_d}{\sqrt{d}}) \right)} - 1 \right\rangle \right] \right)^n \frac{\boldsymbol{\xi}}{\|\boldsymbol{\xi}\|}, \tag{1}$$

where θ is temperature, $\boldsymbol{\xi}$ is the deviatoric relative stress, defined as

$$\boldsymbol{\xi} = \mathrm{dev}(\boldsymbol{\sigma}) - \boldsymbol{\alpha}, \tag{2}$$

and the initial yield strength, $Y(\theta)$, is scaled by a Hall-Petch type factor to account for grain size effects. The isotropic hardening variable, κ, evolves according the following equation:

$$\dot{\kappa} = \left[H(\theta) - R_d(\theta)\kappa \right] \left| \dot{\varepsilon}^p \right| - R_s(\theta)\kappa \sinh\left(Q_s(\theta)\kappa \right) - R_{rex}(\theta) \left[c_k \kappa^2 + c_\alpha \|\alpha\|^2 \right] X^{c_X} \kappa \ , \tag{3}$$

where $H(\theta)$ represents the hardening due to dislocation generation, $R_d(\theta)$ and $R_s(\theta)$ represent dynamic and static recovery, and the last term captures the softening effects of recrystallization. The Jaumann rate of the back stress tensor, $\boldsymbol{\alpha}$, has a similar form:

$$\mathring{\boldsymbol{\alpha}} = h(\theta)\boldsymbol{d}^p - \left[\sqrt{\frac{2}{3}} r_d(\theta) \|\boldsymbol{d}^p\| + r_s(\theta) \right] \sqrt{\frac{2}{3}} \|\boldsymbol{\alpha}\| \boldsymbol{\alpha} - R_{rex}(\theta) \left[c_\kappa \kappa^2 + c_\alpha \|\boldsymbol{\alpha}\|^2 \right] X^{c_X} \boldsymbol{\alpha}. \tag{4}$$

The rate of recrystallization is represented by the evolution of the volume fraction of recrystallized material, denoted by X:

$$\dot{X} = R_{rex}(\theta) \left[c_\kappa \kappa^2 + c_\alpha \|\boldsymbol{\alpha}\|^2 \right] X^{c_X} (1 - X). \tag{5}$$

The form of this equation is based on two assumptions: 1) recrystallization rate is equal to the product of the velocity of the boundaries of recrystallized nuclei and the interfacial area between recrystallized and unrecrystallized regions (see [9,10]); and 2) the velocity of subgrain boundaries is the product of the mobility and the driving pressure (see [11]).

The recrystallization softening terms in the evolution equations for κ and $\boldsymbol{\alpha}$ are derived from the assumption that during static recrystallization, the percent decrease in unrecrystallized volume is equal to the percent reduction in dislocation structure.

The last change to the model is the introduction of a grain size variable to model grain growth (see [12]):

$$\dot{d} = \frac{G(\theta)}{d^m} \tag{3}$$

The temperature-dependent functions in the equations above are defined as follows:

$$n(\theta) = \frac{c_2}{\theta} - c_1 \tag{4}$$

$$Y(\theta) = \frac{c_3}{c_{21} + e^{-c_4/\theta}} \frac{1}{2}\left[1 + \tanh\left(c_{19}\left(c_{20} - \theta\right)\right)\right] \tag{5}$$

$$f(\theta) = c_5 e^{-\frac{c_6}{\theta}} \tag{6}$$

$$r_d(\theta) = c_7 e^{-\frac{c_8}{\theta}} \tag{7}$$

$$h(\theta) = c_9 - c_{10}\theta \tag{8}$$

$$r_s(\theta) = c_{11} e^{-\frac{c_{12}}{\theta}} \tag{9}$$

$$R_d(\theta) = c_{13} e^{-\frac{c_{14}}{\theta}} \tag{10}$$

$$H(\theta) = c_{15} - c_{16}\theta \tag{11}$$

$$R_s(\theta) = c_{17} e^{-\frac{c_{18}}{\theta}} \tag{12}$$

$$Q_s(\theta) = c_{22} e^{-\frac{c_{23}}{\theta}} \tag{13}$$

$$R_{rex}(\theta) = \frac{1}{\theta\mu} e^{-\frac{c_{24}}{\theta}} \tag{14}$$

$$G(\theta) = c_{25} e^{-\frac{c_{26}}{\theta}} \tag{15}$$

Some of the capabilities of the enhanced model are illustrated in Figures 12 and 13. Figure 12 shows that the enhanced model is capable of capturing the softening behavior due to dynamic recrystallization. Figure 13 compares the stress response for two different grain sizes, exhibiting higher yield strengths for finer grain sizes. Figure 14 shows grain growth can be tracked by equation (6). The complete model with changes will be presented in an upcoming paper.

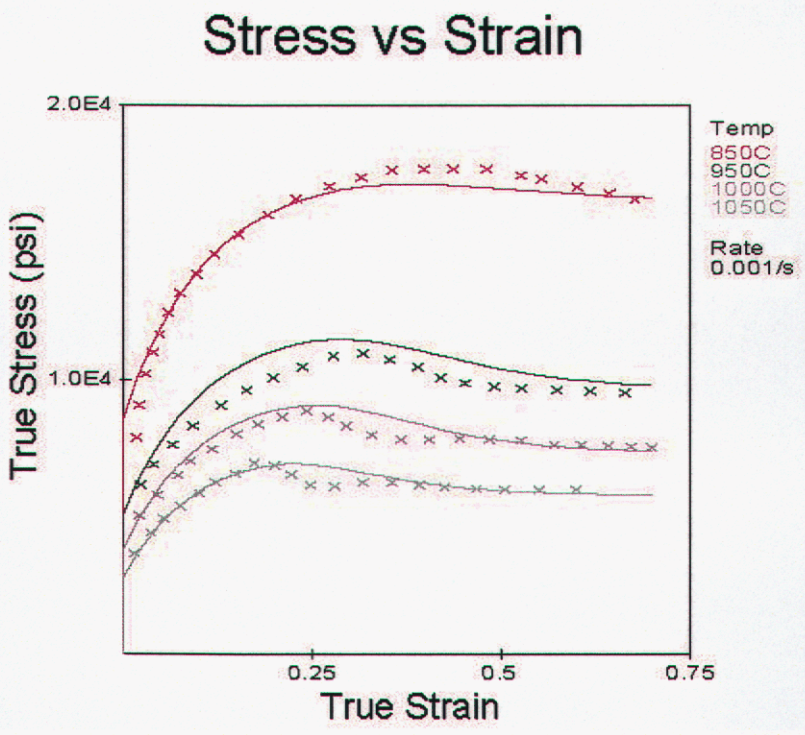

Figure 12 Softening due to dynamic recrystallization (data from [13])

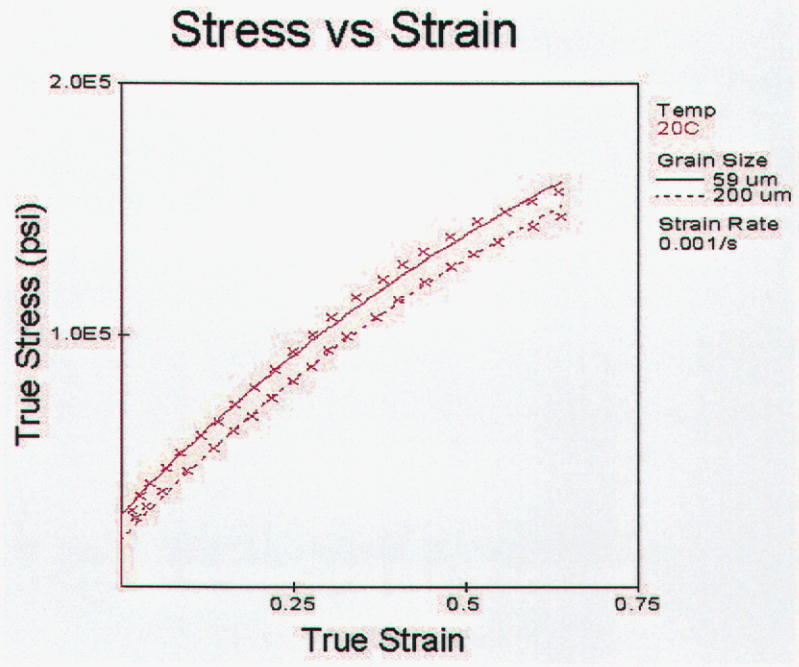

Figure 13 Grain size effects on yield strength (unpublished data from D. Mosher, 1998)

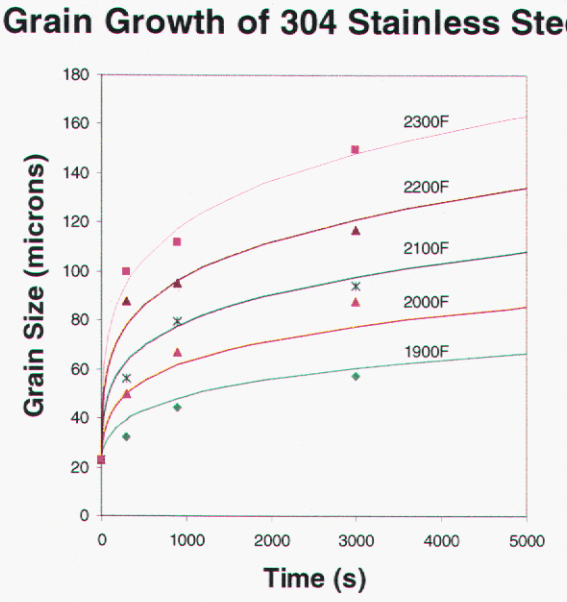

Figure 14 Grain growth at elevated temperatures (data from [14] shown as symbols)

4.2 Transitioning from Sliding to Tied Contact

To enable the bonding of the interface elements in a resistance weld simulation, one further modification was made to the constitutive model: the addition of an integer variable that acts as a binary switch to indicate to the contact algorithm when to transition from sliding to tied contact. Since bond quality in resistance welds is assessed based on the level of recrystallization and grain growth across the interface, the bonding variable in the constitutive model was chosen to be activated when a critical level of recrystallization is reached. The value of the variable changes from 0 to 1 in a given element when the volume fraction of recrystallized material reaches 50%.

In the first generation contact algorithm, to be implemented in FY05, each master surface element will be queried for the switch variable value. If the value is 1, then any nodes on the slave face that are in contact will be tied to the element. The second generation version will only tie a slave node to a master element if both the master element and at least one of the elements to which the slave node belongs have bonding variables that are activated.

4.3 Regression Test

We have provided the SIERRA developers with a simple regression test for switching from sliding to tied contact based on the microstructure evolution. Two blocks are held in contact while they are thermally cycled. The resulting thermal expansion induces plastic strains, recrystallization, and grain growth.

The two blocks (one element each) are in sliding contact at t=0 (see Figure 15). The blocks are both 304L steel, but the top block has a smaller initial grain size. The top surface of the top block and the bottom surface of the bottom block remain fixed in the y direction during the whole simulation. From t=0 to t=125 seconds, the blocks are heated from room temperature to 1350K. They are held at that temperature for 50 seconds, then cooled back to room temperature. Due to thermal expansion, the blocks are compressed, leading to plastic deformation, recrystallization, and grain growth. The finer grain size of the top block gives rise to a higher yield strength, thus the plastic strain and resulting recrystallization are slightly retarded compared to the weaker bottom block. The bottom block reaches the critical level of recrystallization at 136 seconds, whereas the top follows at 156 seconds. The state variable indicator for switching from sliding to tied contact switches from 0 to 1 in the top and bottom blocks at 156 and 136 seconds, respectively. As the blocks are cooled down to room temperature, they separate. This is because the heights of both blocks are shortened due to the plastic deformation.

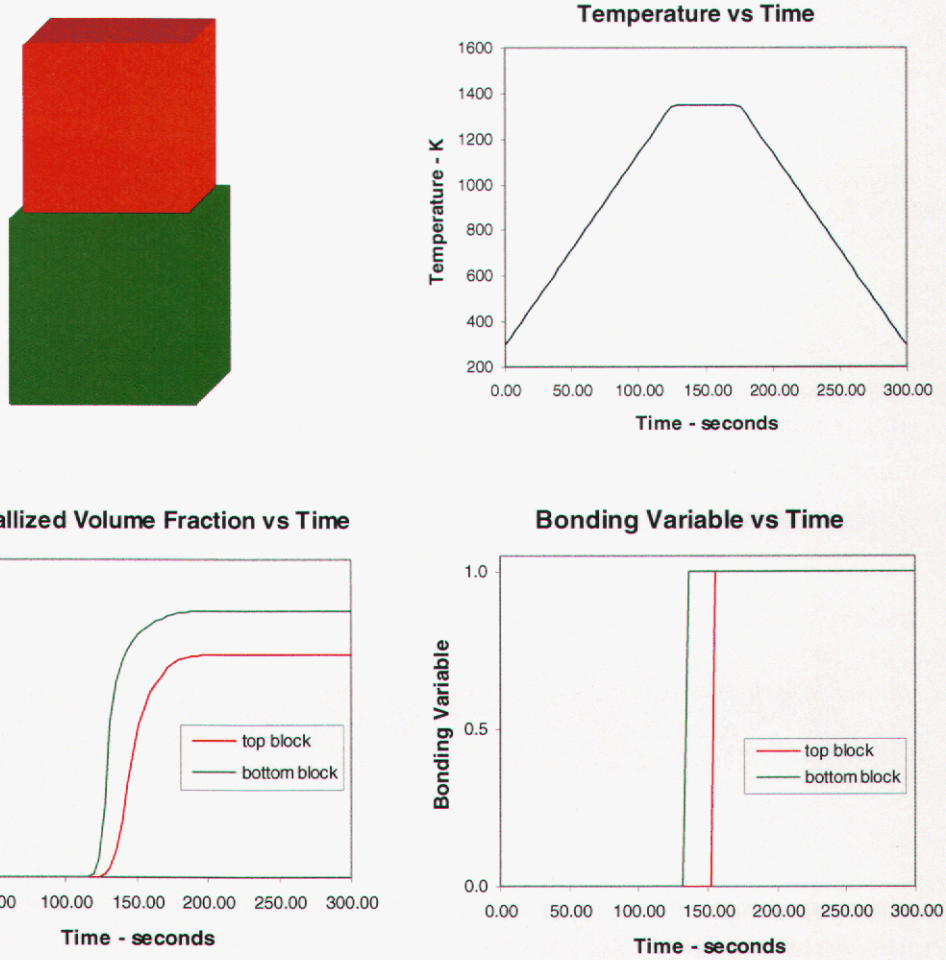

Figure 15 Regression test for transition from sliding to tied contact

Once the SIERRA developers have implemented the transition from sliding to tied contact based on STATE_BCJ_MEM_13, this cooling stage will show that the two blocks remain connected and hence will be pulled in tension. For the first generation implementation, the nodes of the top block (slave) will be tied to the bottom block (master) at 136 seconds, when the bond switch activates in the bottom block. For the second generation implementation, the nodes will not tie until 156 seconds, when both blocks are activated.

4.4 Future Modifications

The effectiveness of the recrystallization model will be tested in FY05 using new Sandia C6 data. Two possible enhancements that may be required are: 1) the addition of a term in the grain size evolution equation to account for the grain refinement that can occur during recrystallization at high strain rates, and 2) the inclusion of a misorientation variable related to the lattice mismatch across the geometrically necessary subgrain boundaries. The subgrain boundaries play a fundamental role in the nucleation process during recrystallization, and hence the initiation and rate of recrystallization may depend heavily on the misorientation variable. In the nonlocal plasticity model of Regueiro et al. [15], geometrically necessary dislocations are modeled using the curl of the elastic part of the deformation gradient. In the local EMMI model, we would first attempt to capture the salient effects with a scalar measure, although the misorientation variable should ultimately be a second order tensor.

This page intentionally left blank

5 The Sandia Tapered Bar Problem

Personnel in Department 01833 are utilizing a specially instrumented Gleeble to perform two C6 experiments in support of the ASCI AD resistance weld modeling effort. We refer to these tests as the Sandia tapered bar (STB) experiment and the Sandia tapered butt weld (STBW) experiment. (See Figure 2 and the related discussion).

The STB experiment is similar to the Eggert-Dawson experiment [2] that motivated the acceptance problem. The major differences are the size and composition of the specimen, the way in which the current is applied, and the measurement used to determine the electrical boundary condition.

The dimensions of the Sandia tapered bar are shown in Figure 16. The specimen is approximately 50 percent larger than the one used in the acceptance problem. Because of power source limitations in the Sandia tests, an AC electrical field is used as opposed to the DC field used in the Eggert-Dawson experiments [2]. Furthermore, in simulations of the STB experiments, measured voltage is used as the eCALORE electrical boundary condition as opposed to a measured current. In the Sandia tests, measured voltage is significantly more accurate than measured current. Since the electrical power input to the specimen is proportional to the square of the current, the voltage measurement was deemed to be a better choice for the electrical boundary condition. Unfortunately, as we discuss later, utilizing the measured AC voltage boundary condition proved to be problematic.

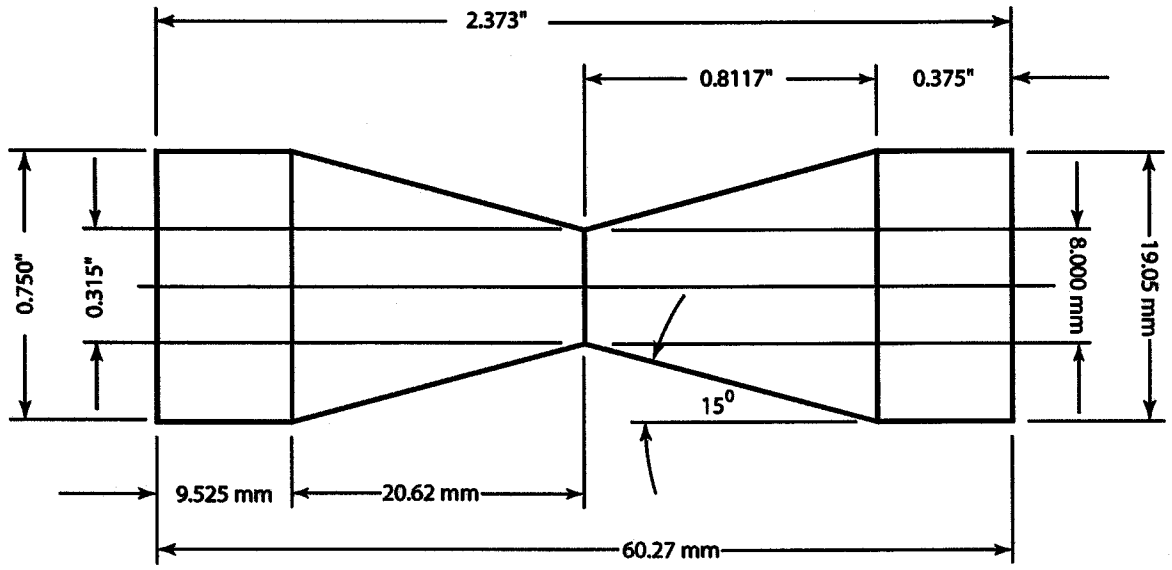

Figure 16 Sandia tapered bar specimen

Unlike the Eggert-Dawson experiments, the Sandia specimens are fabricated from well-characterized annealed 304L stainless steel. Furthermore the Sandia experiments will culminate in the measurement of residual stresses that can be compared to those predicted by CALAGIO simulations.

The mesh for the STB problem is shown in Figure 17. As was the case for the acceptance problem, symmetry considerations permitted us to use a mesh that encompasses only one eighth of the entire tapered bar. The flat faces parallel to the XY and YZ planes are mechanical symmetry planes that are thermally and electrically insulated. The face in the XZ plan at the specimen waist is also a mechanical symmetry plane with thermal insulation and a voltage potential of zero. The larger surface that is parallel to the XZ plane represents the specimen end. At this surface one half of the experimentally measured voltage (specimen end-to-end measurement) is applied. The measured axial pressure is also applied here and a fixed temperature equal to the initial room temperature is provided for the thermal boundary condition. The remaining cylindrical curved surfaces, which represent the outer surface of the specimen, are mechanically free to deform and are electrically insulated. Heat loss due to thermal grey-body radiation is simulated for the thermal boundary condition.

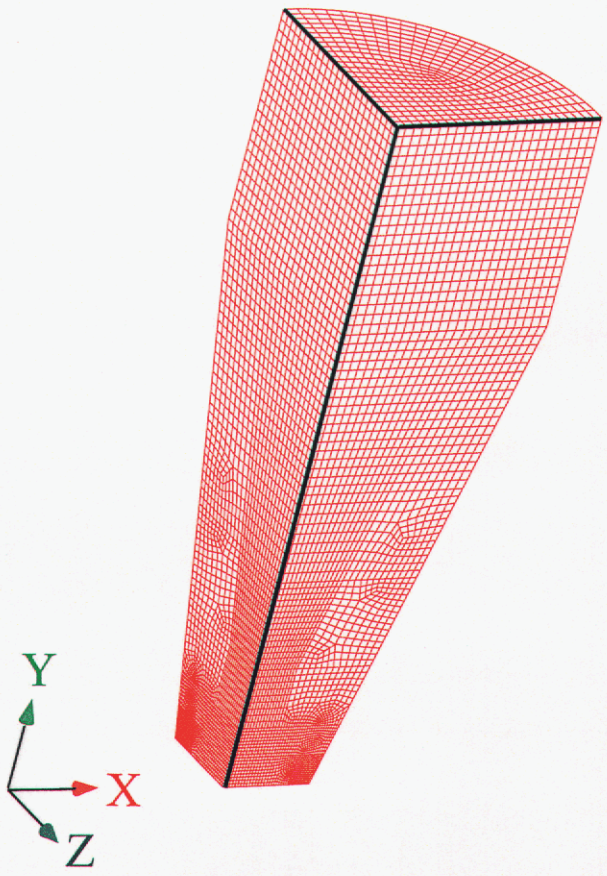

Figure 17 Medium mesh for Sandia tapered bar problem

A CALAGIO simulation of the C6 STB Test #7 was performed using the mesh shown in Figure 17. Figure 18 shows one half of the measured peak to peak AC voltage applied to the specimen during Test #7. For the CALAGIO simulation, this transient voltage was applied to the specimen end using a piecewise linear curve constructed from a long series of voltage-time data points. The CALAGIO simulation began at t=0 (time zero) with the application of the measured axial pressure. At two seconds the transient voltage is applied for approximately 0.4 seconds. The simulation is continued for a cool down period that lasts until t=5.0 seconds. The measured axial pressure is applied for the entire five seconds.

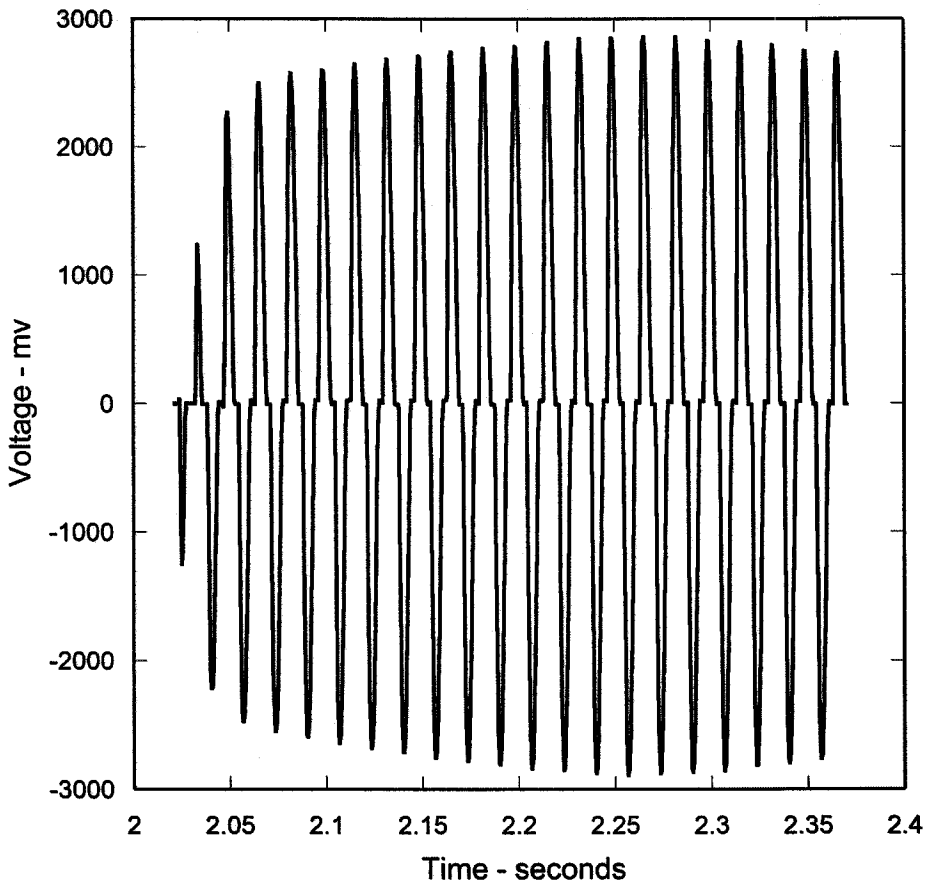

Figure 18 eCALORE voltage boundary condition for alternating current (C6 Test #7)

Three meshes were used to simulate the STB problem. We refer to these meshes as the "very coarse", "coarse" and "medium" meshes. Statistics for these meshes are summarized in Table 3. The mesh previously shown in Figure 17 is the medium mesh. The final deformed medium mesh is shown in Figure 19. This is the state of the mesh at t=5.0 seconds. The "bulge" at the specimen waste is clearly visible.

Table 3 STB Mesh Statistics

Mesh	Number of Nodes	Number of Elements
Very Coarse	2521	1968
Coarse	15744	15744
Medium	57829	53136

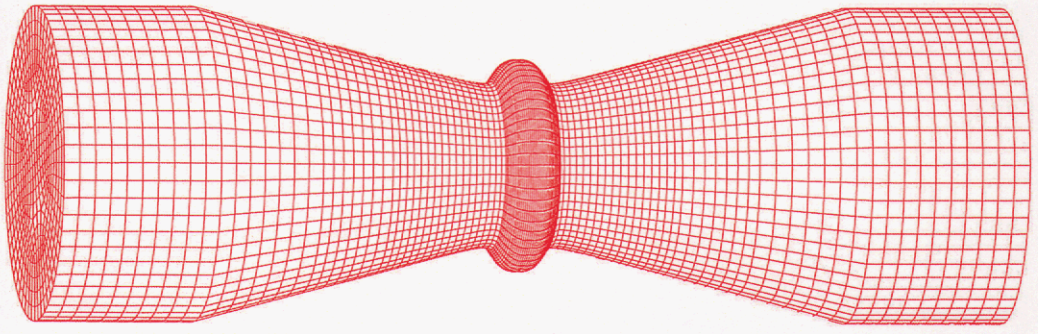

Figure 19 Final deformed mesh for Sandia tapered bar problem

Figure 20 shows how specimen temperature, upset and equivalent plastic strain evolves during the CALAGIO simulation of C6 Test #7. The series of colored hourglass shapes running from left to right along the upper part of the figure are mid-plane cross-sections of temperature distribution. Time is assumed to proceed from left-to-right. The corresponding cross-sections for equivalent plastic strain are shown on the bottom of the figure. By following the red lines from the cross-sections to the plot in the center of the figure, it is possible to relate the various distributions to the upset history. The heat generation near the specimen waist for $2.0 < t < 2.4$ and the subsequent cool-down due to heat conduction and thermal radiation is clearly evident in the temperature cross-sections. The region that undergoes plastic deformation is confined to the middle (waist) of the specimen. It is shown in red in the plastic strain cross-sections. The region of plastic strain is highly localized. The shortening of the specimen with time can be seen from the upward movement of the bottom boundary in each hourglass cross-section.

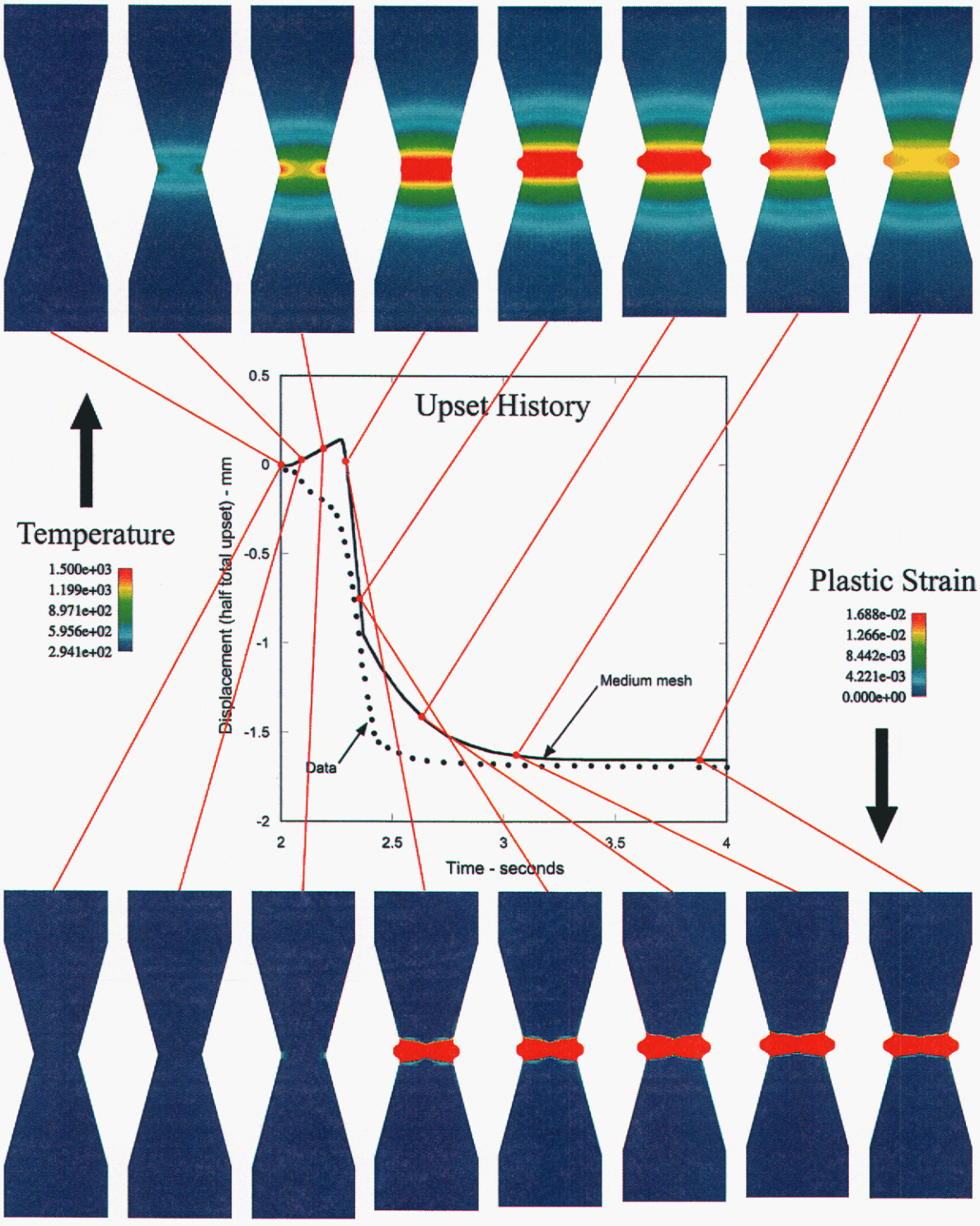

Figure 20 Temperature (K) and plastic strain history during upset

Figure 21 illustrates that the CALAGIO simulation of C6 Test #7 is approaching mesh convergence. The predictions for time evolving specimen offset are compared for the three meshes described in Table 3. Also shown is the measurement for specimen offset. Differences between the simulations and the data are most evident in two areas. The first is the time period $0 < t < 2.3$ where the prediction shows a specimen elongation due to thermal elastic expansion. During this same period the data shows a specimen length reduction consistent with an earlier transition to plastic flow. The second area of model-data disagreement is the time period $2.4 < t < 3.0$ immediately after the voltage is turned off. The prediction shows a more gradual upset to the final deformed shape than does the data.

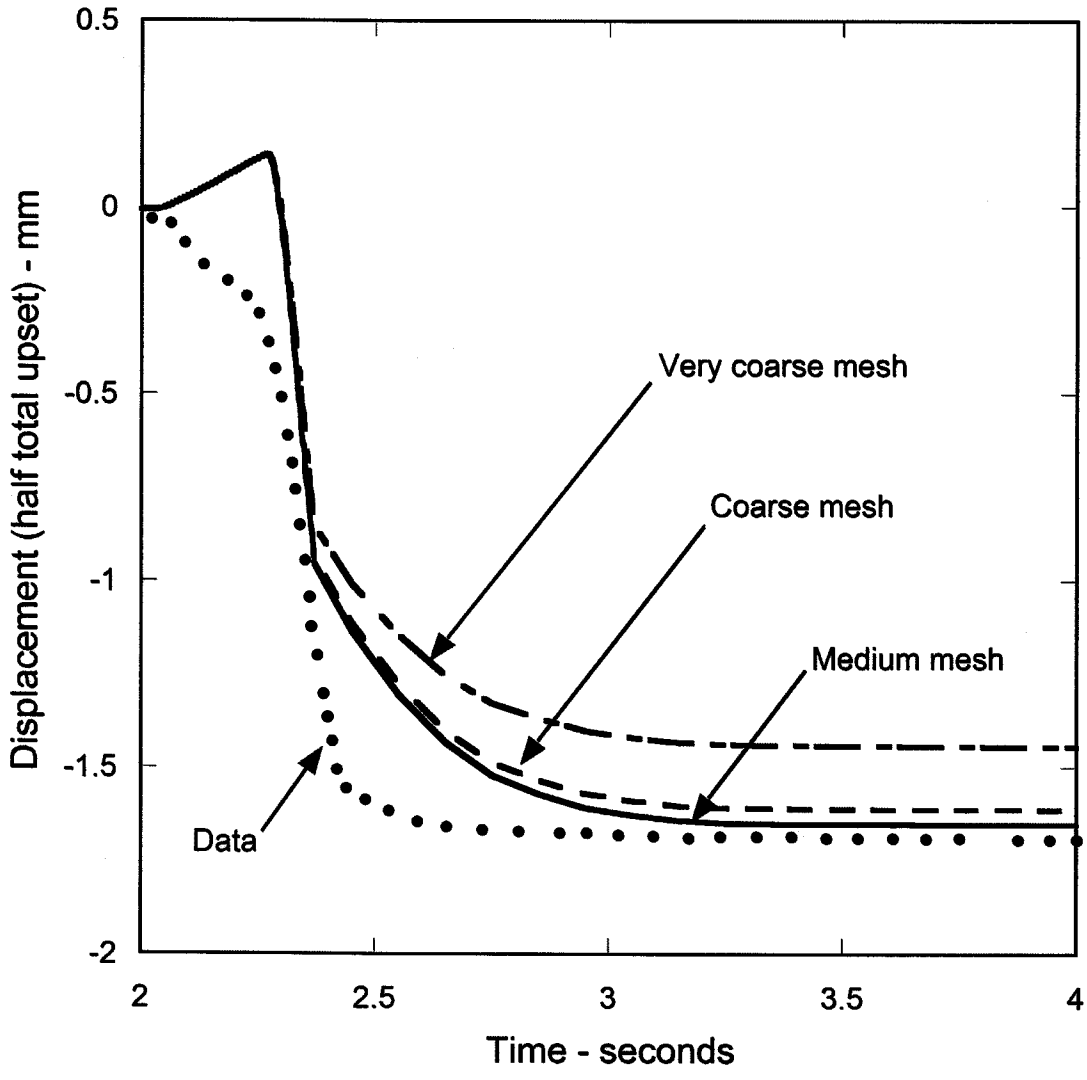

Figure 21 Mesh convergence for the Sandia tapered bar problem

There is some concern regarding the accuracy of the C6 measurements and how these measurements were used to develop boundary conditions for the CALAGIO simulation. The most serious of these has to do with the measurement of specimen end-to-end voltage. When the measured voltage was used as a boundary condition, the simulation predicted peak to peak current flows approaching 15,000 amps. The Gleeble power supply is known to be current limited at 10,000 amps, indicating that the current flow in the actual experiment could not have been as great as that predicted. This discrepancy led to an examination of how the specimen end-to-end voltage measurement was made.

Figure 22 shows the specimen and two copper end caps which are part of the specimen clamping system. The copper end caps serve two purposes. The first is to provide a reliable registration reference to insure that the specimen centerline is precisely aligned along the axis of the Gleeble. The second is to provide a connecting point for the power supply electrodes. In the current configuration, the end-to-end voltage measurement is made at the copper end caps and not at the specimen ends. Utilizing such a voltage measurement as the specimen end-to-end boundary condition assumes a negligible electrical contact resistance between the copper end caps and the specimen. Unfortunately, the predictions of current flow would seem to indicate that the voltage applied at the copper end caps significantly exceeds the voltage at the specimen boundaries; in other words there appears to be a significant contact resistance between the end caps and the specimen. In order to test this theory, the measured current was examined. Even with some experimental error in the current measurement, this current fell far short of the values consistent with the voltage measurement indicating the presence of significant interface resistance.

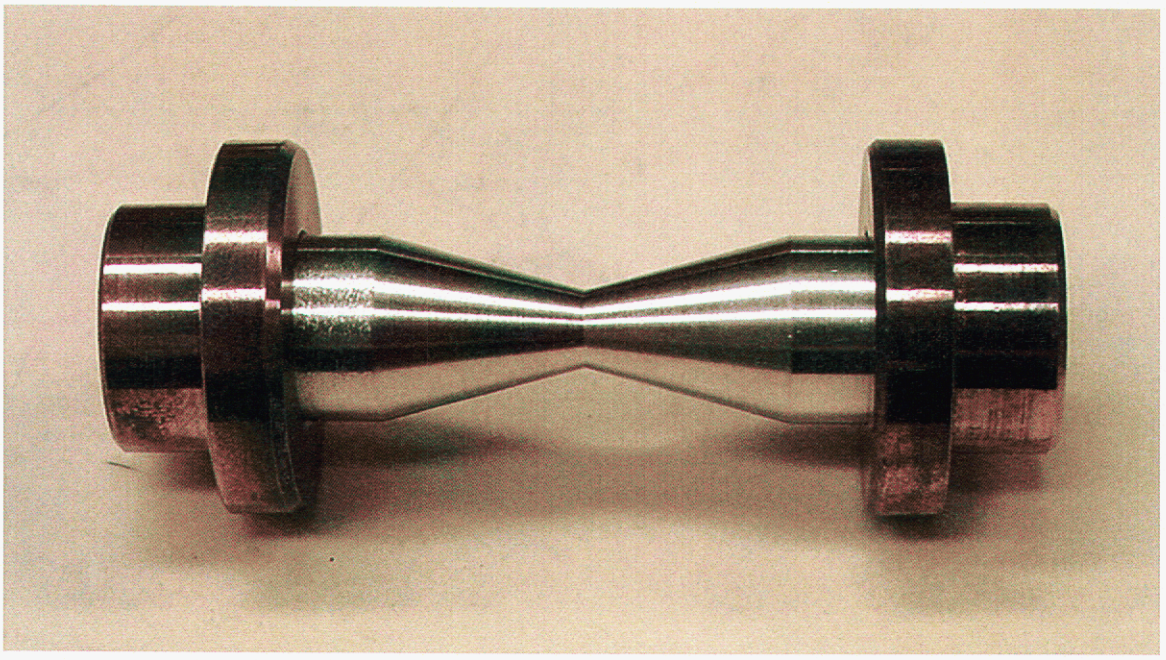

Figure 22 Specimen and copper electrode end caps

In light of the uncertainties in measuring specimen end-to-end voltage, an alternate method must be found to specify electrical boundary conditions for the simulation. The most straightforward method would be to improve the accuracy of the measured current. This would permit a specified current density to be used as the electrical boundary condition at the specimen ends. An alternative to this approach is to provide attachment points for voltage measurement along the straight sections of the specimen. This approach was successfully demonstrated by Eggert and Dawson [2] in their experiments.

6 Summary and Conclusions

This report has documented activities for the third year of the multiyear Resistance Weld Process Modeling AD Project. During this year we successfully demonstrated a mesh and time step converging solution to the tapered bar Acceptance Problem. This represents the first significant three-way (electrical-thermal-mechanical) coupled solution using the SIERRA tool CALAGIO (eCALORE, CALORE, ADAGIO driver). Our CALAGIO predictions for the Acceptance Problem compare favorably with measurements made by Eggert and Dawson [2-4].

We completed a number of tests using the new higher order SD3DH8 element. This selective deviatoric element has the potential to render converged solutions with fewer elements than the single-point quadrature UG3DH8 element. Our tests have shown that the SD3DH8 element is extremely sensitive to mesh quality and coarseness. Its behavior is unpredictable and solutions frequently exhibit unacceptable levels of hourglassing (spurious energy modes). We will continue to work with the developers to understand and improve the behavior of this element so that it can eventually be applied to coupled thermal-mechanical problems.

We examined a number of methods to improve convergence of coupled thermal-mechanical problems using the UG3DH8 element. A matrix of problems was run using various values of parameters related to element strain formulation, preconditioner type, and hourglass control. We found that whenever the strongly objective strain formulation was used, either hourglassing or the lack of convergence errors occurred. When the midpoint-increment strain formulation was used, neither of these problems arose and stable solutions were achieved. This finding was reported to the SIERRA developers. As a result, an error was discovered in the calculation of effective moduli used in hourglass routines with the strongly objective strain formulation. The error has been corrected and as of now, the UG3DH8 element is satisfying our needs providing stable solutions free of hourglassing.

A number of new features were added to the EMMI constitutive model to enable it to predict the solid state bonding process. Evolution variables were added to track recrystallization and grain growth. In addition an integer variable was incorporated into the constitutive model to determine when recrystallization and grain growth is sufficient to cause a solid state bond. The new variable acts as a binary switch to indicate to the contact algorithm when to transition from sliding to tied contact thus effecting a bond. A simple regression test was designed so that the SIERRA developers could test their implementations for sliding to tied contact based on microstructural evolution. This feature will be needed early next year when we begin to simulate the tapered bar butt weld problem.

Work was begun on simulating the Sandia Tapered Bar Experiment. This C6 experiment is being conducted on an instrumented Gleeble where current, voltage, offset and temperatures will be measured. The experiment is similar to the tapered bar Acceptance problem except that it will conclude with the measurement of residual stresses that can be compared to CALAGIO predictions. Several meshes were built for the STB problem and we have demonstrated a near mesh convergent solution. Significant uncertainties exist in applying measured voltages as boundary conditions for the simulations. We are working with the C6 principle investigator to resolve these problems.

This page intentionally left blank.

Appendix A

Application of TORO-COYOTE-JAS to Resistance Welding

Introduction

This appendix summarizes the analysis and material modeling effort conducted in this ASC AD project prior to FY03 where a parallel, coupling of the finite element codes TORO (electrical),[1,2] COYOTE (thermal),[3,4] and JAS (structural)[5,6] was used. The staggered coupling procedure is summarized in Ref. 7 and is not repeated here.

In this study, the process model is applied to a problem that mimics the resistance butt-welding of 304 stainless steel tapered bars. Experimental data exists from a previous study[8] in which both large load and high current were applied to a single, tapered bar (an interface did not exist). This configuration allows us to concentrate on the fundamental issues of electrical-thermal-mechanical coupling, as well as the large deformation and high temperature material response, without complicating the problem with uncertainties related to modeling contact issues, i.e., contact resistance effects and solid state bonding.

Material Model

The model used in the analysis is a finite deformation internal state variable model based upon the thermally activated motion of dislocations, and is therefore inherently strain rate and temperature dependent. The kinematics of deformation is described by a multiplicative decomposition of the deformation gradient into elastic and plastic parts. Two internal state variables are introduced – a scalar representing statistically stored dislocations (SSDs) and a tensor to describe the effects of geometrically necessary dislocations (GNDs) or compatibility dislocations. Specific details of the model can be found in Ref. 9. Most of the work hardening in the model is associated with the evolution of the SSDs. Following Kocks and Mecking,[10] during an increment of plastic strain, $d\varepsilon_p$, the dislocation density, ρ_{ss}, increases inversely proportional to the mean free path, l, and recovers proportional to the density of SSDs,

$$\frac{d\rho_{ss}}{d\varepsilon_p} = \frac{c_1}{l} - c_2\rho_{ss} \tag{1}$$

Since the mean free path for the dislocations is inversely proportional to the square root of the density of SSDs, equation (1) can be written,

$$\frac{d\rho_{ss}}{dt} = \left(c_1\sqrt{\rho_{ss}} - c_2\rho_{ss}\right)\dot{\varepsilon}_p - c_3\rho_{ss}Sinh\left[\overline{Q}_s(\theta)\sqrt{\rho_{ss}}\right] \tag{2}$$

In equation (2), the final term has been added to account for static recovery and $\overline{Q}_s(\theta)$ has a nonlinear dependence upon temperature. The internal strength κ, associated with the SSDs is given in Ref. 11 as

$$\kappa = c_4 \mu(\theta) b \sqrt{\rho_{ss}} \tag{3}$$

where b is the Burger's vector and μ(θ) is the temperature dependent shear modulus,

$$\mu(\theta) = \mu_0 \left\{ 1 + \frac{(\theta - 300)}{\theta_m} \frac{\theta_m d\mu}{\mu_0 d\theta} \right\} \tag{4}$$

μ_0 is the shear modulus at 300K, θ_m is the melt temperature, which is 1670K for 304 SS, and the temperature dependence of the modulus $(\theta_m/\mu_0)(d\mu/d\theta)$ is –0.85. Taking the time derivative of (3) and solving for $\dot{\rho}_{ss}$

$$\dot{\rho}_{ss} = \frac{2\dot{\kappa}\sqrt{\rho_{ss}}}{c_4 \mu b} - c_4 \frac{\partial \mu}{\partial \theta} \dot{\theta} b \sqrt{\rho_{ss}} \tag{5}$$

Then, equating equation (5) with equation (2), along with the expression for ρ_{ss} from equation (3), the evolution of the internal strength becomes,

$$\dot{\kappa} = \{H(\theta) - R_d(\theta)\kappa\}|\dot{\varepsilon}_p| - R_s(\theta)\kappa Sinh[Q_s(\theta)\kappa] + \frac{\kappa}{\mu(\theta)} \frac{d\mu(\theta)}{d\theta} \dot{\theta} \tag{6}$$

Where,

$$H(\theta) = \frac{c_1 c_2 \mu b}{2}; R_d(\theta) = \frac{c_2}{2}; R_s(\theta) = \frac{c_3}{2}; Q_s(\theta) = \frac{\overline{Q}_s(\theta)}{c_4 \mu b} \tag{7}$$

Therefore, $H(\theta)$ has the same linear temperature dependence as the shear modulus and $R_d(\theta)$, $R_s(\theta)$ and $Q_s(\theta)$ are assumed to follow an Arrhenius temperature dependence. The last term describes the relaxation of the internal elastic stress field with increasing temperature. This term, although often neglected, can have a dominant effect in problems involving very rapid heating or cooling.

Consider a block of material with an initial residual strength (from prior deformation) of 288 MPa. Based upon previous weld simulations, the material is allowed to expand freely during a temperature ramp from 294K to 1600K in 0.2s. This results in a temperature rate of $6530 Ks^{-1}$. Figure 1 illustrates the effect of the elastic relaxation (ER) of the internal stress field on the decrease in internal strength. Without the effect of elastic relaxation, the internal strength does not change until around 0.15s when the thermal recovery results in an abrupt drop in strength.

Consideration of the effects of elastic relaxation yields an immediate linear drop in the internal strength until 0.15s when thermal recovery again becomes the dominant softening mechanism. This mechanism is extremely important in the weld analysis to be considered in this work.

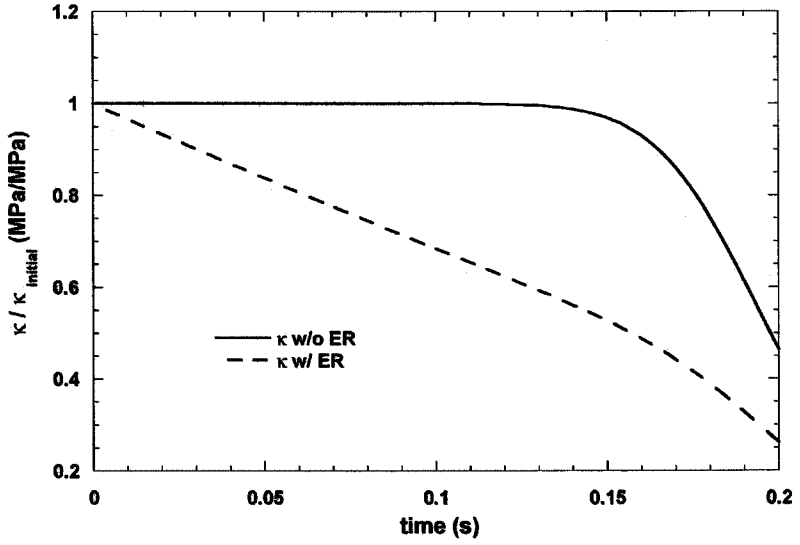

Fig. 1: Effect of elastic relaxation (ER) on the internal strength due to rapid heating

Results

Although our ultimate goal is the prediction of residual stresses due to resistance upset welding, accurate simulation of the thermal and deformation histories was judged to be critical in assessing the performance and development of the process model. Therefore, predicted thermal and mechanical results were compared with experimental data from a previous study[8] in which both large load and high current were applied to a single, previously worked, tapered bar.

Figure 2 shows the geometry of the specimen. One of the numerous 3-D finite element meshes used in this study is shown in Fig. 3. Although the geometry and boundary conditions are axisymmetric, only a 3-D electrical-thermal-mechanical predictive capability exists. In the analysis, all nodes at the mid-length of the bar (i.e., the bottom surface in Fig. 3) were restrained from moving in the axial direction, but were free to move in the symmetry plane. In addition, the heat flux and voltage were zero at this plane. Symmetry was applied to both internal surfaces along the length of the bar and a radiation boundary condition was specified on the exterior of the bar. On the top surface in Fig. 3 or end of the bar, the measured axial load and current (Fig. 4) were applied with a spatially uniform distribution and a constant temperature (294.15K) was specified.

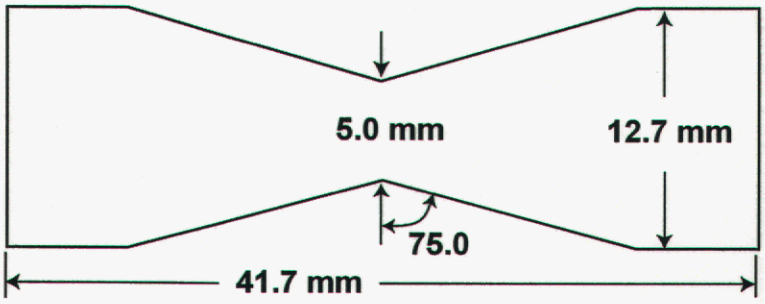

Fig. 2: Dimensions of specimen
The tapered bar design is axisymmetric about the longitudinal axis.

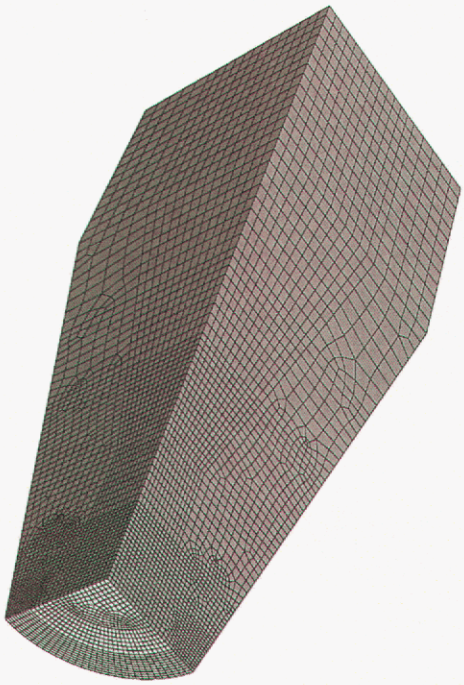

Fig. 3: Finite element mesh containing 45,699 nodes and 41,946 elements

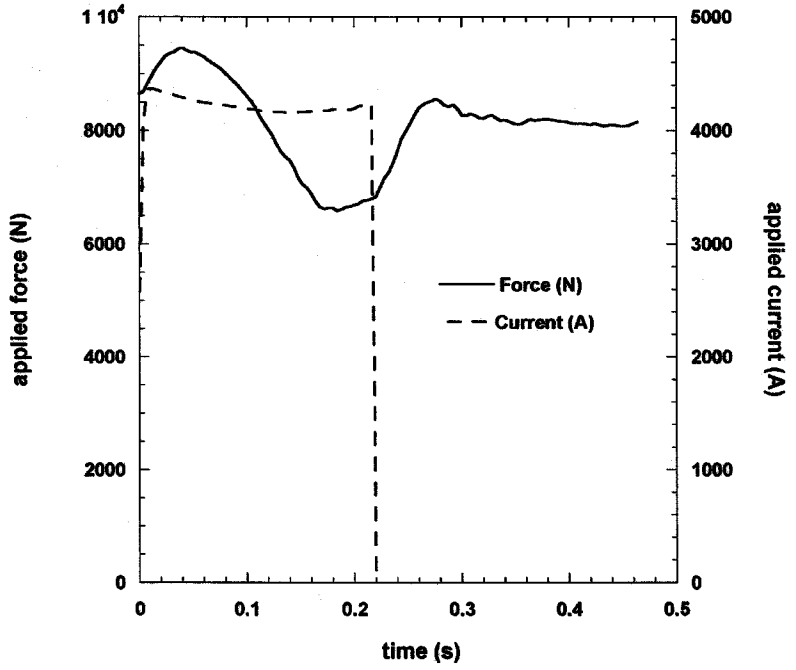

Fig. 4: Measured load and current boundary conditions applied to ends of tapered bar. Data taken from Ref. 12.

The 304 SS parameters for the material response model were determined by fitting the model to tension and compression mechanical property data spanning a wide range of temperatures and strain rates.[13] Because the bar had been previously worked, the internal strength, κ, was initialized to reflect the statistically stored dislocations. Prior experimental studies[14] indicated that the total strength of the bar stock was 480 MPa. Because the intrinsic yield strength at room temperature is 192 MPa, the remaining strength was lumped into κ (288 MPa). The temperature dependent electrical and thermal properties for 304 SS were obtained from Ref. 12. Thermal expansion and elastic properties as a function of temperature were taken from Refs 15 and 16, respectively.

Initial electrical-thermal-mechanical simulations of the tapered bar problem employing a medium density mesh (45699 nodes) revealed up to a 10% error between the computed and measured thermal results.[7] The source of the discrepancy of these preliminary results was traced to using a form of the material model that did not include the softening effects of elastic relaxation, ER, discussed earlier. Figures 5 and 6 illustrate experimental and model comparisons for the temperature and deformation, respectively. Neglecting ER delayed the onset of axial (Fig. 6) and radial deformation. The reduced deformation early in time results in greater current densities, increased Joule heating, and higher peak temperatures (Fig. 5). On the other hand, including ER enabled the material to immediately soften and deform. Early agreement with the global, axial deformation resulted in a more accurate prediction of the thermal response at thermocouple T2 (Fig. 5). Re-examining Figure 1 in light of the tapered bar simulations provides clarification. The heating rate and time scale for the simple example (Fig. 1) were similar to the conditions at thermocouple T2. Consequently, the time scale for axial deformation in the tapered bar simulation neglecting ER can be correlated with thermal recovery and the abrupt drop in strength. The simulation of the tapered bar incorporating ER paralleled the simple example by exhibiting an immediate drop in the internal strength until thermal recovery became the dominant softening mechanism. Clearly, incorporating elastic relaxation was needed to successfully predict the experimental findings.

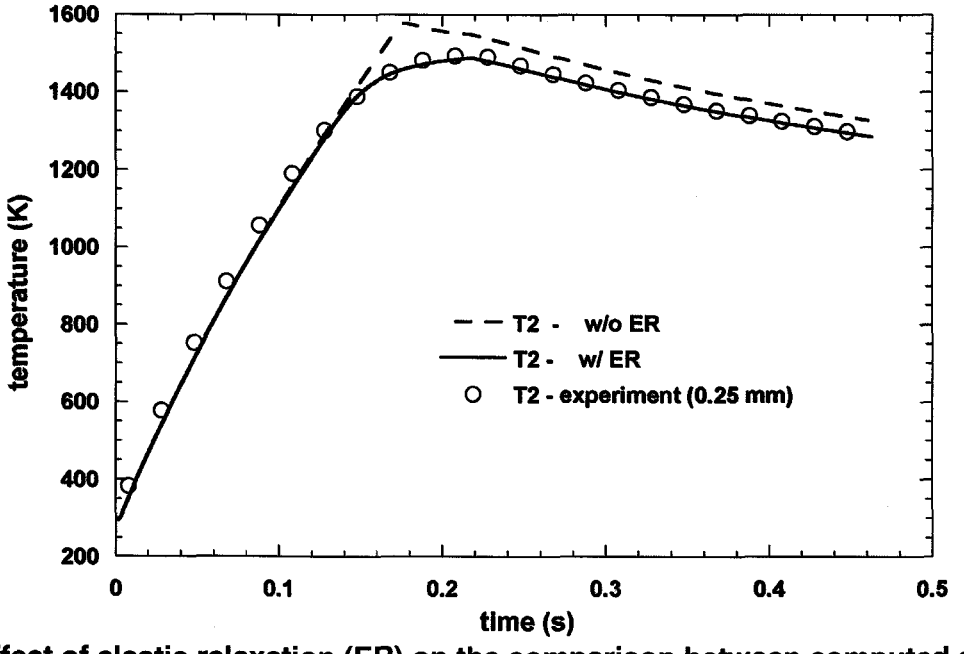

Fig. 5: Effect of elastic relaxation (ER) on the comparison between computed and measured temperature histories at 0.25 mm from the mid-length of the bar. Computed results employed medium density mesh, i.e., 45699 nodes.

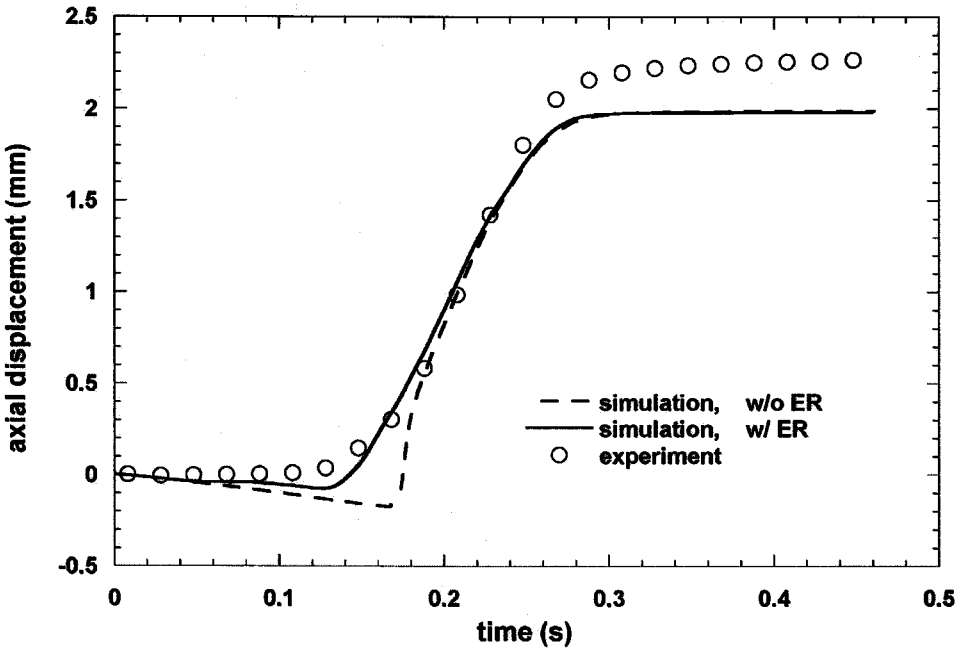

Fig. 6: Effect of elastic relaxation (ER) on the comparison between computed and measured axial displacement results. Computed results employed medium density mesh, i.e., 45699 nodes.

For completeness, numerous coupled simulations were performed with decreasing time step and element size. The adaptive time step error tolerance was decreased in successive simulations until the predicted temperature field converged. In addition, four different finite element mesh densities consisting of 4642 nodes, 45699 nodes, 246248 nodes, and 732498 nodes were employed to establish convergence of the predicted results. Convergence of the calculated results is confirmed in Fig. 7, which compares computed axial displacement results for the four mesh densities against measured data. Lastly, excellent agreement (less than 5% error) was achieved between the predicted thermal and experimental results (Fig. 8), and the calculated and measured final deformed shape (Fig. 9) for the highest fidelity mesh.

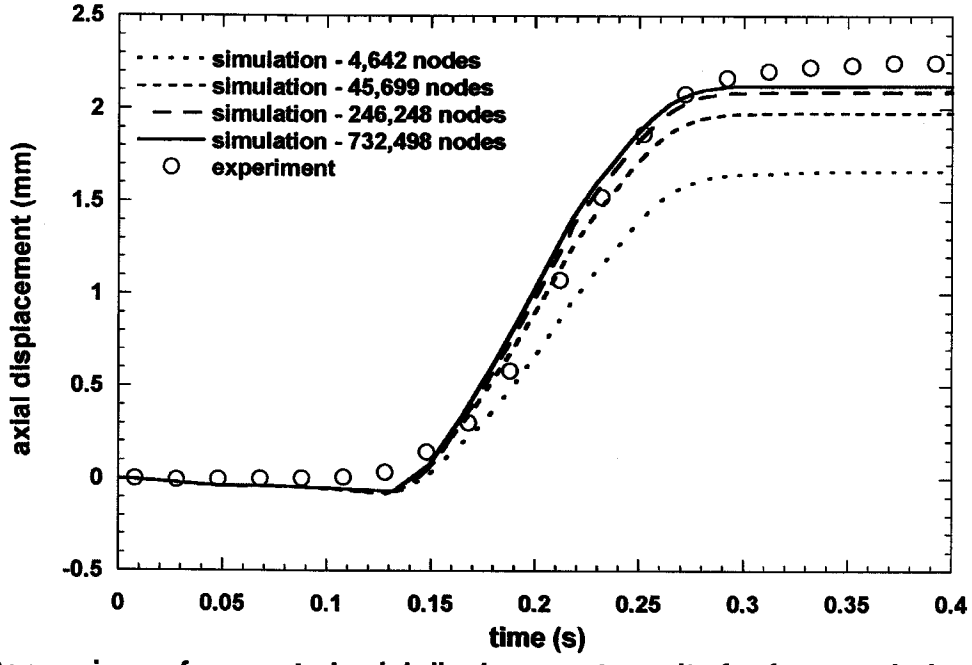

Fig. 7: Comparison of computed axial displacement results for four mesh densities with experimental data

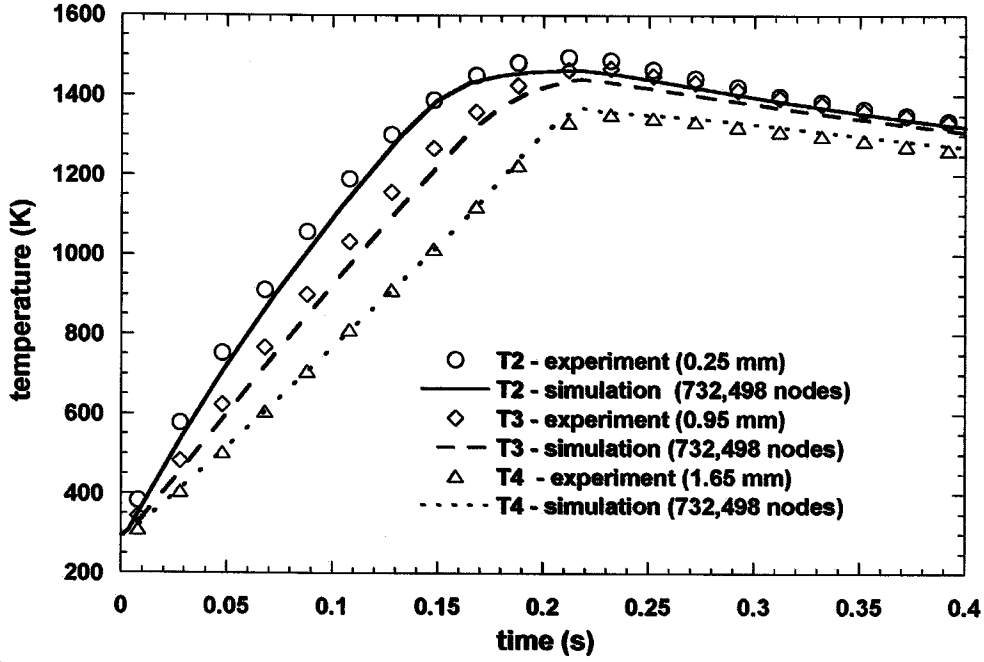

Fig. 8: Comparison of predicted and measured temperature histories. Thermocouples T2, T3, and T4 were located 0.25 mm, 0.95 mm, and 1.65 mm from the mid-length of the bar.

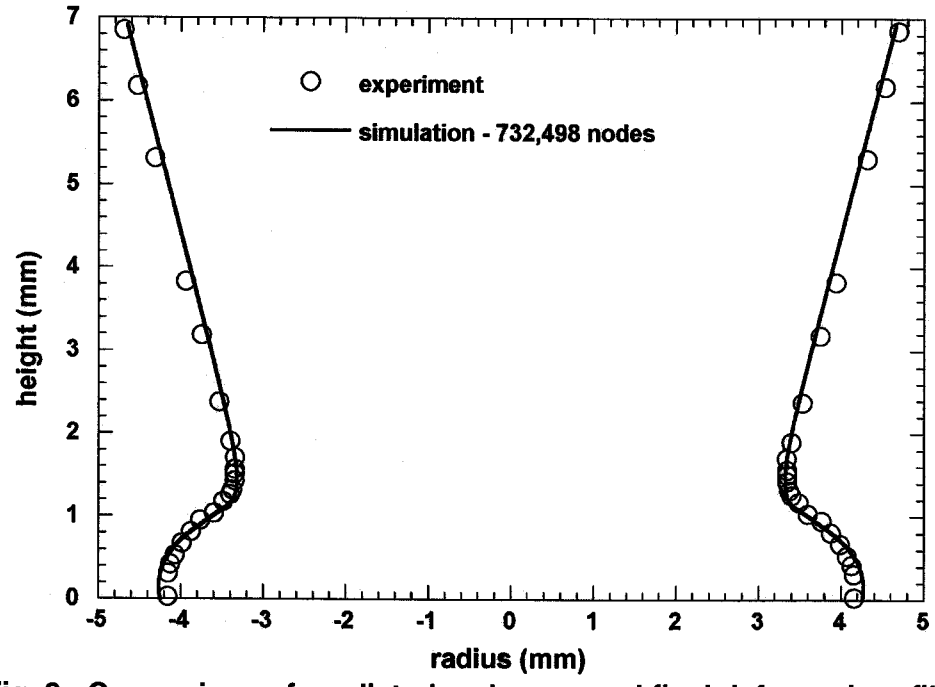

Fig. 9: Comparison of predicted and measured final deformed profile

References for Appendix A

1. D. K. GARTLING: "TORO—A Finite Element Computer Program for Nonlinear, Quasi-Static Problems in Electromagnetics, Part I—Theoretical Background, Version 4.0", Report SAND 95-2472, Sandia National Laboratories, Albuquerque, NM, 2001.
2. D. K. GARTLING: "TORO—A Finite Element Computer Program for Nonlinear, Quasi-Static Problems in Electromagnetics, Part II—User's Manual, Version 4.0", Report SAND 96-0903, Sandia National Laboratories, Albuquerque, NM, 2001.
3. D. K. GARTLING, R. E. HOGAN, and M. W. GLASS: "COYOTE—A Finite Element Computer Program for Nonlinear Heat Conduction Problems, Part I—Theoretical Background, Version 4.0", Report SAND 94-1173, Sandia National Laboratories, Albuquerque, NM, 2001.
4. D. K. GARTLING, R. E. HOGAN, and M. W. GLASS: "COYOTE—A Finite Element Computer Program for Nonlinear Heat Conduction Problems, Part II—User's Manual, Version 4.0", Report SAND 94-1179, Sandia National Laboratories, Albuquerque, NM, 2001.
5. J. H. BIFFLE: "JAC3D—A Three-Dimensional Finite Element Computer Program for the Nonlinear Quasistatic Response of Solids with the Conjugate Gradient Method", Report SAND87-1305, Sandia National Laboratories, Albuquerque, NM, 1993.
6. M. L. BLANFORD: "JAS3D User's Instructions, Release 1.6", Internal memorandum, Sandia National Laboratories, Albuquerque, NM, August, 12, 1998.
7. A. R. ORTEGA, J. W. FOULK III, M. L. CHIESA and D. K. GARTLING: "Development of Validated Resistance Weld Modeling Tools", 6th ASME-JSME Thermal Engineering Joint Conference, Hapuna, Kauai, Hawaii, 2003.
8. G. M. EGGERT and P. R. DAWSON: "Assessment of a Thermoviscoplastic Model of Upset Welding by Comparison to Experiment", Int. J. Mech. Sci., 1986, 28 (9), 563-589.
9. D. J. BAMMANN, M. L. CHIESA, and G. C. JOHNSON: "Modeling Large Deformation and Failure in Manufacturing Processes", Theoretical and Applied Mechanics 1996, T. Tatsumi, E. Watanabe, and T. Kambe eds, Elsevier Applied Science, New York, NY, 1997.
10. H. MECKING and U. F. KOCKS: "Kinetics of Flow and Strain-Hardening", Acta Metallurgica, 1981, 29 (11), 1865-1875.
11. G. I. TAYLOR: "The Mechanism of Plastic Deformation of Crystals", Proceedings of the Royal Society, 1934, A145, 362-415.
12. G. M. EGGERT: "A Large Strain Thermomechanical Forming Model for Elastic-Viscoplastic Behavior in Metals", Ph. D. diss., Cornell University, Ithaca, NY, 1987.
13. J. F. LATHROP: "BFIT—A Program to Analyze and Fit the BCJ Model Parameters to Experimental Data", Report SAND97-8218, Sandia National Laboratories, Livermore, CA, 1996.
14. G. M. EGGERT and P. R. DAWSON: "On the Use of Internal State Variable Constitutive Equations in Transient Forming Processes", Int. J. Mech. Sci., 1987, 29 (2), 95-113.

15. Y. S. TOULOUKIAN and C. Y. HO eds, "Thermophysical Properties of Selected Aerospace Materials, Part II", CINDAS, Purdue University, Lafayette, IN, 1977.

16. A. R. ORTEGA, J. J. DIKE, J. F. LATHROP, C. H. CADDEN, D. R. FOLK and J. E. ROBLES: "Analysis and Validation of Multi-Pass Girth Welds in Pipes", Modeling of Casting, Welding and Advanced Solidification Processes VIII, San Diego, California, 1998.

This page intentionally left blank.

References

[1] D. J. Bammann, M.L. Chiesa, and G.C. Johnson, "Modeling Large Deformation and Failure in Manufacturing Processes," Theoretical and Applied Mechanics 1996, T. Tatsumi, E. Watanabe, and T. Kambe eds., Elsevier Applied Science, New York, NY, 1997.

[2] G.M. Eggert and P.R. Dawson, "Assessment of a Thermoviscoplastic Model of Upset Welding by Comparison to Experiment," *Int. J. Mech. Sci.*, Volume 28, Number 9, pp. 563-589, 1986.

[3] G.M. Eggert and P.R. Dawson. "On the Use of Internal Variable Constitutive Equations in Transient Forming Processes," *Int. J. Mech. Sci.*, Volume 29, Number 2, pp. 95-113, 1987

[4] G.M. Eggert and P. R. Dawson, "A Viscoplastic Formulation with Elasticity for Transient Metal Forming," *Computer Methods in Applied Mechanics and Engineering*, Volume 70, pp. 165-190, 1988.

[5] A.R. Ortega, J.W. Foulk III, M.L. Chiesa, and D.K. Gartling "Development of Validated Resistance Weld Modeling Tools," The 6th ASME-JSME Thermal Engineering Joint Conference, March 16-20, 2003.

[6] J.W. Foulk III, A.R. Ortega, and D.J. Bammann, "The Importance of Modeling Elevated Temperature Material Response and Large Deformation in Resistance Upset Welds," 7th International Numerical Analysis of Weldability Conference, Graz, Austria, September 30, 2003.

[7] Adagio User Documentation - User's Guide Version 1.07, Sandia National Laboratories, 2004.

[8] D. J. Bammann, "Modeling the Temperature and Strain Rate Dependent Large Deformation of Metals," *Applied Mechanics Review*, Volume 43, No. 5, pp. 312-319, May 1990.

[9] J.W. Cahn and W. Hagel, in Decomposition of Austenite by Diffusional Processes, Interscience, New York, 1960.

[10] G. R. Speich and R. M. Fisher, in Recrystallization, Grain Growth and Textures, ed. H. Margolin, ASM, 563, Metals Park, Ohio (1966)

[11] F.J. Humphreys and M. Hatherly, Recrystallization and related annealing phenomena, New York, 1995

[12] M. Hillert, "On Theory Of Normal And Abnormal Grain Growth," Acta Metallurgica (1965), v.13, no.3, p.227

[13] F. Montheillet and J. Le Coze, "Influence of purity on the dynamic recrystallization of metals and alloys," *Physica Status Solidi A*, Volume 189, Number 1, pp. 51-58, 2002.

[14] J.K. Stanley and A.J. Perrotta, "Grain growth in austenitic stainless steels," *Metallography*, Volume 2, Number 4, pp. 349-362, 1969.

[15] R.A. Regueiro, D.J. Bammann, E.B. Marin, and K. Garikipati, "A Nonlocal Phenomenological Anisotropic Finite Deformation Plasticity Model Accounting for Dislocation Defects," *ASME Journal of Engineering Materials and Technology*, Volume 124, Number 3, pp.380-387, 2002.

Distribution

External:

Professor R.O. Ritchie
Ernest Orlando Lawrence Berkeley National Laboratory
MailStop 62-203
1 Cyclotron Road
Berkeley, CA 94720

Professor G.C. Johnson
Mechanical Engineering
6149 Etcheverry Hall
University of California
Berkeley, CA 94720-1740

Internal:

1	MS 0889	M. F. Hosking, 1813
1	MS 0889	G. A. Knorovsky, 1813
1	MS 0427	S. E. Klenke, 2118
1	MS 1310	J. A. Mitchell, 2614
1	MS 9001	M. E. John, 8000
		Attn: R. H. Stulen, 8100
		D. R. Henson, 8200
		T. A. Michalske, 8300
1	MS 0914	K. R. Hughes, 8242
1	MS 0914	A. R. Ortega, 8242
1	MS 9108	C. H. Cadden, 8243
1	MS 9108	S. L. Robinson, 8243
1	MS 9403	J. M. Hruby, 8700
1	MS 9404	G. D. Kubiak, 8750
		Attn: S. W. Allendorf, 8753
		J. A. Lamph, 8755
1	MS 9409	P. A. Spence, 8754
1	MS 9409	N. R. Moody, 8754
1	MS 9042	B. R. Antoun, 8754
1	MS 9160	W. R. Even, 8760
		Attn: D. L. Medlin, 8761
		T. J. Shepodd, 8762
		J. L. Lee, 8764
1	MS 9049	E. P. Chen, 8763
1	MS 9049	D. J. Bammann, 8763
5	MS 9049	A. A. Brown, 8763
2	MS 9405	J. W. Foulk, 8763
1	MS 9049	R. E. Jones, 8763
1	MS 9049	P. A. Klein, 8763

1	MS 9405	E. B. Marin, 8763
1	MS 9405	H. S. Park, 8763
1	MS 9405	R. A. Reguerio, 8763
1	MS 9049	J. A. Zimmerman, 8763
1	MS 9405	K. L. Wilson, 8770
		Attn: J. C. F. Wang, 8773
		N. Y. C. Yang, 8773
1	MS 9402	J. E. M. Goldsmith, 8772
1	MS 9402	J. D. Puskar, 8772
1	MS 9042	D. Kwon, 8774
		Attn: J. J. Bhutani, 8774
		M. Burger, 8774
		J. A. Crowell, 8774
		M. A. Forman, 8774
		R. D. Gilbert-O'Neil, 8774
		Y-R Kan, 8774
		C. J. Kimmer, 8774
		R. J. Mariano, 8774
		Y. Ohashi, 8774
		V. D. Revelli, 8774
		R. R. Settgast, 8774
		T. R. Shelton, 8774
		N. Spencer, 8774
		L. I. Weingarten, 8774
1	MS 9042	M. L. Chiesa, 8774
1	MS 9042	J. J. Dike, 8774
1	MS 9154	S. E. Gianoulakis, 8774
1	MS 9042	M. D. Jew, 8774
1	MS 9042	B. L. Kistler, 8774
1	MS 9042	D. L. Kletzli, 8774
5	MS 9042	W. S. Winters, 8774
1	MS 9409	C. B. Moen, 8775
1	MS 9409	W. G. Houf, 8775
1	MS 9409	G. J. Wagner, 8775
1	MS 0151	A. C. Ratzel, 9100
		Attn: W. L. Hermina, 9110
		J. S. Lash, 9114
		B. Hassan, 9115
		R. O. Griffith, 9117
		P. J. Wilson, 9120
		J. M. Redmond, 9124
		T. J. Baca, 9125
		R. A. May, 9126
		T. Y. Chu, 9130
1	MS 0836	E. S. Hertel, 9116
1	MS 0836	B. L. Bainbridge, 9116

1	MS 0893	J. Pott, 9123
1	MS 0893	C. S. Lo, 9123
1	MS 0893	W. M. Scherzinger, 9123
1	MS 0372	J. Jung, 9127
1	MS 0372	J. T. Ostien, 9127
1	MS 0372	G. W. Wellman, 9127
1	MS 0382	J. H. Strickland, 9141
1	MS 0382	S. W. Bova, 9141
1	MS 0382	M. W. Glass, 9141
1	MS 0382	R. L. Lobar, 9141
1	MS 0380	K. F. Alvin, 9142
1	MS 0380	N. K. Crane, 9142
1	MS 0380	A. S. Gullerud, 9142
1	MS 0380	J. D. Hales, 9142
1	MS 0380	K. H. Pierson, 9142
1	MS 0382	J. R. Stewart, 9143
1	MS 0899	Technical Library, 9616
3	MS 9018	Central Technical Files, 8945-1
1	MS 9021	Classification Office, 8511 for Technical Library, MS 0899, 9616
	MS 9021	Classification Office, 8511 for DOE/OSTI via URL